DILATANCY BASED CALCULATION OF LATERAL EARTH THRUST AND THE LOCKED-IN STRESS CONCEPT

by

Ahmet Talha Gezgin

B.S., Civil Engineering, Boğaziçi University, 2012

Submitted to the Institute for Graduate Studies in
Science and Engineering in partial fulfillment of
the requirements for the degree of
Master of Science

Graduate Program in Civil Engineering
Boğaziçi University

2015

DILATANCY BASED CALCULATION OF LATERAL EARTH THRUST AND THE LOCKED-IN STRESS CONCEPT

APPROVED BY:

Assoc. Prof. Özer Çinicioğlu (Thesis Supervisor)	.....
Assist. Prof. Ece Bayat	.....
Prof. Erol Güler	.....

DATE OF APPROVAL: 07 January 2015

To my family

ACKNOWLEDGEMENTS

I would like to express my gratitude to all the people who in one way or another contributed to the development of this research.

First and foremost, my sincere appreciation and gratitude goes to my supervisor Assoc. Prof. Özer Çinicioğlu for his valuable help in instructing, sharing of knowledge, guiding and supporting me throughout the duration of this thesis.

Also, I extend my sincere thanks to the members of my Master's thesis examination committee: Prof. Erol Güler and Assist. Prof. Ece Bayat for their kind and supportive attitude towards me and in depth comments and advice.

My gratitude also goes to my colleagues at Bogaziçi University. Special thanks to Behzad Soltanbeigi, Adlen Altunbaş, Emirhan Sancak, Cihan Cengiz, Utku Takmaz and Mert Öztürk for their assistance in the experiments, discussions, and sharing the ideas.

Above all, I would like to thank my family for their personal support and great patience at all times. My parents and my brothers have given me their endless support throughout the thesis, as always they do.

Finally I would like to express my gratitude to The Scientific and Technological Research Council of Turkey (TUBITAK) for supporting my research through Project number 110M595.

ABSTRACT

DILATANCY BASED CALCULATION OF LATERAL EARTH THRUST AND THE LOCKED-IN STRESS CONCEPT

Precise calculation of the loads and stresses that are acting on structures that are interacting with soils is central to the design of geotechnical structures. Accordingly, calculation of vertical soil stresses is a straightforward task whereas computation of lateral stresses is a topic of ongoing research. Conventional design methods for retaining structures consider the ultimate lateral earth pressures, namely active and passive earth pressures. As it is clearly identified in geotechnical literature, strength of backfills and the shapes of the failures planes control the magnitudes of active and passive thrust on retaining structures. Accordingly, this study attempts to come up with a precise method for the calculation of active and passive earth thrusts. For this purpose, a new equation (Altunbaş 2014) that uses dilatancy angle for the calculation of the geometry of the active failure plane is incorporated into the method of slices for the computation of active earth thrust. Accuracy of the proposed method is checked using the results obtained from small-scale physical retaining wall model tests. The same approach is repeated for passive earth thrust. Differences between the computed and measured results are discussed and the reasons for the differences are discussed theoretically. A new concept called locked-in stresses is developed to consider elastically stored residual normal stresses in soil bodies and their influences strength.

ÖZET

YATAY ZEMİN ETKİSİNİN GENLEŞİM AÇISINA BAĞLI HESAPLANMASI VE KENETLENME GERİLİMİ KAVRAMI

Zeminle etkilesim içerisinde olan yapilara etkiyen yükler ve gerilmelerin hassas hesaplanmasi, geoteknik yapilarinin tasariminda esastir. Bu nedenle, yatay gerilmelerin hesaplanmasinin devam eden çalismalarin bir konusu oldugu için, düsey zemin gerilmelerinin hesaplanmasi açik bir görevdir. Istinat yapilari için klasik tasarim yöntemleri, aktif ve pasif toprak basinçlari olarak adlandirilan nihai yatay toprak basinçlarini göz önüne alir. Geoteknik literatüründe açikça belirtildigi üzere, istinat yapilarina uygulanan aktif ve pasif itkilerin büyüklüklerini dolgularin mukavemeti ve göçme yüzeylerinin sekilleri kontrol eder. Bundan dolayi, bu çalisma aktif ve pasif zemin itkilerinin hesaplanmasi için hassas bir yöntem önermeye çalismaktadir. Bu amaçla, aktif göçme yüzey geometrisinin hesaplanmasi için genlesim açisini kullanan yeni bir esitlik (Altunbaş 2014), aktif toprak itkilerinin hesaplanmasi için dilim yönteminin içerisine katilmistir. Önerilen yöntemin dogrulugu küçük ölçekli istinat duvari modeli deneylerinden elde edilmis sonuçlar kullanilarak kontrol edilmistir. Ayni yaklasim pasif zemin etkisi için tekrarlanir. Hesaplanan ve ölçülen sonuçlar arasindaki farklar ve farklarin sebepleri teorik yönden karsilastirilmistir. Ayrica, önerilen yöntemin pasif toprak itki hesaplamalarina uygulanmasi da degerlendirilmistir. Zemin içerisinde elastik olarak biriken kalici normal gerilimler ve onlarin mukavemete etkisini göz önüne almak için, kenetlenme gerilimi olarak adlandirilan yeni bir kavram gelistirilmistir.

TABLE OF CONTENTS

ACKNOWLEDGEMENTS iv
ABSTRACT v
ÖZET vi
LIST OF FIGURES ix
LIST OF TABLES xiv
LIST OF SYMBOLS xv
LIST OF ACRONYMS/ABBREVIATIONS xvii
1. INTRODUCTION 1
1.1. Theory Background 1
2. LITERATURE REVIEW 2
2.1. Active Earth Pressure 2
2.2. Small Scale Retaining Wall Model 7
2.3. Dilatancy Angle and Peak Friction Angle of Cohesionless Soils 10
2.4. Method of Slices 11
2.5. Ordinary Method of Slices 11
2.5.1. Simplified Bishop Method 13
2.5.2. Spencer's Method 14
2.5.3. Janbu's Simplified Method 15
2.5.4. Janbu's Rigorous Method 16
2.5.5. Morgenstern-Price Method) 18
2.6. General Limit Equilibrium Methods for the computation of Lateral Earth Thrust 20
3. TESTING METHODOLOGY 22
3.1. Properties of the Small Scale Retaining Wall Model 22
3.2. Properties of the Testing Sand 25
3.3. Direct Shear Test 26
3.3.1. Test Procedure 27
3.4. Data Analysis 28
3.5. Placement of the Backfill in the Small Scale Retaining Wall Model . . . 30

3.6. Conducting the Tests in the Small Scale Retaining Wall Model 31
4. VISUALIZATION OF FAILURE IN ACTIVE STATE 33
4.1. Quantification of Failure Surface Geometry 39
4.2. Determination of the Failure Surface Geometry Based on Dilatancy Angle 40
5. A NEW METHOD TO CALCULATE THE ACTIVE FORCES ACTING ON THE WALL 45
5.1. Identifying the Slope Angle of the Base of the Slice 46
5.2. Identifying The Shear Force on the base of the Slice and the Friction Force between the Backfill and the Plexiglass Surface 48
5.3. Identifying the Weight of a Slice 49
5.4. Interslice Force Function for the Active Earth Force 50
5.5. Identifying the Normal Force Acting at the Base of the Slice 52
6. THE RESULTS FOR ACTIVE LATERAL EARTH THRUSTS 55
6.1. Calculated Active Thrust Magnitudes 56
6.2. Measured Active Thrust Magnitudes 56
6.3. Results for the Values of Active Lateral Earth Forces Acting on the Wall According to Rankine and Coloumb Theories 56
7. CALCULATION OF PASSIVE FORCES ACTING ON THE WALL BY USING THE NEW METHOD 58
7.1. Passive Failure Surface Geometries 58
7.2. Interslice Function at Passive State 60
7.3. Normal Force Acting at Base of a Slice 60
7.4. Passive Lateral Earth Thrust Acting on the Wall 61
7.5. The Results For Passive Lateral Earth Thrusts 61
7.6. Locked-in Stress Concept 63
8. DISCUSSION 69
8.1. Active Lateral Earth Thrusts 69
8.2. Passive Earth Thrust 71
9. CONCLUSIONS 74
REFERENCES 75

LIST OF FIGURES

Figure 2.1. Coloumb theory for Active Earth Pressure. 2

Figure 2.2. Rankine theory for Active Earth Pressure. 3

Figure 2.3. Stress Redistribution Caused by Arching (Paik and Salgado, 2003). 4

Figure 2.4. Trajectory of Minor Principal Stresses in Granular fill at Ditch (Paik and Salgado, 2003). 5

Figure 2.5. Trajectory of Minor Principal Stresses in Backfill Behind Retaining Wall (Paik and Salgado, 2003). 6

Figure 2.6. Mohr Circle for Stresses at Wall (Paik and Salgado, 2003). 6

Figure 2.7. Layout of Experimental Setup (Hanna and Khoury (2005). 8

Figure 2.8. Location of Transducers on Retaining Wall (Hanna and Khoury 2005). 8

Figure 2.9. Transducers Box Unit Used to Measure Vertical Stresses in Sand Mass (Hanna and Khoury (2005). 9

Figure 2.10. Slices with Forces Considered in the Ordinary Method of Slice. . . 11

Figure 2.11. Forces Actually Actingon the Slice in the Ordinary Method of Slice. 12

Figure 2.12. Slices with Forces Considered in Simplified Bishop Method. 13

Figure 2.13. Slices with Forces Considered in Spencer's Method. 14

Figure 2.14. Slices with Forces Considered in Simplified Janbu Method. 16

Figure 2.15. Slices with Forces Considered in Janbu's Rigorous Method. 17

Figure 2.16. Functional Variation of the Direction of the Side Force with Respect to the x Direction. 19

Figure 2.17. Possible Interslice Force Functions for a Horizontal Backslope: (i) Active Case, (ii) Passive Case (From Rahardjo and Fredlund 1984). 21

Figure 3.1. Experimental Set-Up. 22

Figure 3.2. Crossectional view of the Physical Model. 23

Figure 3.3. The Location of Pressure Transducers and Transparent Side Walls. 23

Figure 3.4. The Back Face of the Retaining Wall. 24

Figure 3.5. The Data Acquisition System. 24

Figure 3.6. Sieve Analysis of Tested Sand. 25

Figure 3.7. Vibratory Table Used to Determine Maximum Minimum Void Ratios. 25

Figure 3.8. The Samples of (i) The Model Retaining Wall, (ii) The Plexiglass, and (iii) The Sand Paper. 27

Figure 3.9. Preparation of Direct Shear Test. 28

Figure 3.10. Direct Shear Test Results for (i) The Wall Model-Backfill Interface, (ii) Plexiglass-Backfill Interface and (iii) Sandpaper-Backfill Interface. 29

Figure 3.11. Placement of the Sand by Pluviation Method. 30

Figure 3.12. Placement of Density Cans on the Backfill. 30

Figure 3.13. The Compaction Method. 31

Figure 3.14. The Image Capture During the Test. 32

Figure 4.1. Determination of Displacement Vector Field (i) Pixel Intensity Variation Signature (ii) Displacement Vector. 33

Figure 4.2. Triangular Element Mesh for Strain Calculation Plotted in X_y Coordinates. Note That Because Some "Wild" Vectors Were Evident in the Displacement Plots, the Associated Patches Have Been Removed From the Element Mesh (Jackson 2010). 34

Figure 4.3. Patch Size Effect on Geopiv Results. 35

Figure 4.4. Typical PIV Results for Active Retaining Wall Translation (i) Shear Strain (ii) Volumeti Strain (iii) Vector Field (iv) Deformed Patches Profile. 36

Figure 4.5. Localization of Cumulative Strains In Initially Dense Sand Based on as Obtained From PIV Analyses (a) Distribution of Shear Strains (ε_s), b) Distribution of Volumetric Strains (ε_v), (b) Vector Field of Deformation. 37

Figure 4.6. Shear Strain Concentration and Failure Surface Evolution with Respect to Rigid Retaining Wall Movement. 38

Figure 4.7. Localization of cumulative strains in initially loose sand as obtained from PIV analyses (a) shear strain (ε_s), (b) volumetric strains (ε_v), (c) vector field of deformation. 39

Figure 4.8. Detection of the Failure Surface Geometry a) As Plotted on the Shear Strain Map b) As Shown with an Illustration. 40

Figure 4.9. Shape of the Assumed 2nd Order Parabolic Failure Surface (Altunbaş 2014). 42

Figure 4.10. a_b-tan(ψ_p) Relationship Obtained Using the Data Gathered From Retaining Wall Model Study (Altunbaş 2014). 42

Figure 4.11. The Comparison of the Tests in Which the Wall and the Wall With Sand Paper for (i) Loose Bacfill (ii) Medium Dense Backfill and (iii) Dense Backfill. 44

Figure 5.1. Forces Acting on Soil Mass in Active Failure State. 45

Figure 5.2. The Forces Acting on a Slice on the Failure Surface in Active Case. 46

Figure 5.3. The Coordinates of the Base Corners of n^{th} Slice. 47

Figure 5.4. The Length from the Starting Point of the Failure Surface to a Desired Point on the Failure Surface. 50

Figure 5.5. The Interslice Function for Active Case. 51

Figure 5.6. The Assumed Common Length for Right and Left Sides of the Slice. 53

Figure 7.1. Passive Failure Surface Geometry Dependent on Dilatancy Angle. 58

Figure 7.2. a_b-tan(ψ_p) Relationship Obtained Using the Data Gathered From Retaining Wall Model Study for Passive Cases (Altunbaş 2014). . 59

Figure 7.3. The Results for the Calculated and Measured Passive Lateral Thrusts. 63

Figure 7.4. Soil Particles in a Tank (i) Before the Compaction (ii) After the Compaction. 64

Figure 7.5. Lateral Earth Pressure Coefficient at Rest for Each Test. 65

Figure 7.6. The Results for the Recalculated and Measured Passive Lateral Thrusts. 68

Figure 8.1. The Relationship Between Dilatancy Angle and Active Lateral Earth Thrust According to Calculation Results, Measurement Results and Rankine Theory. 69

Figure 8.2. The Relationship Between Dilatancy Angle and Active Lateral Earth Thrust According to Calculation Results, Measurement Results and Coloumb Theory. 70

Figure 8.3. The Relationship Between Dilatancy Angle and Passive Lateral Earth Thrust According to Calculation Results, Measurement Results and Rankine Theory. 72

Figure 8.4. The Relationship Between Dilatancy Angle and Passive Lateral Earth Thrust According to Calculation Results, Measurement Results and Coloumb Theory. 73

LIST OF TABLES

Table 3.1. The Properties of Tested Sand. 26

Table 6.1. The Common Parameters for all the Tests. 55

Table 6.2. The Specific Parameters of the Backfills Prepared for Active Tests. 55

Table 6.3. The Results for Active Lateral Earth Thrusts Obtained from the Calculation Method, the Measurement Method, and Rankine and Coloumb Theories. 57

Table 7.1. The Specific Parameters of the Backfills Prepared for Passive Tests. 62

Table 7.2. The Results for the Calculated and Measured Passive Lateral Thrusts. 62

Table 7.3. The Results for the Recalculated and Measured Passive Lateral Thrusts. 68

LIST OF SYMBOLS

a_b	is defined as the ratio of B_f to x
b	the width of the n^{th} slice
c'	effective cohesion
$E_R - E_L$	horizontal interslice forces acting on the right and left sides of the slice, respectively
F	factor of safety
S_m	the shear force
F_S	the friction force between the backfill and the side surface of the tank whose material is plexiglass
FS	Factor of Safety
$f(x)$	functional variation respect to, horizontal distance from the slice to the center of rotation
K_0	lateral earth pressure coefficient at rest
$(K_o)_{comp}$	lateral earth pressure coefficient at rest in compacted cohesionless soils
N	the normal force on the base of the slice
$(p_i)_{comp}$	initial mean effective stress in compacted cohesionless soils
$(p_i)_{nc}$	initial mean effective stress in normally-compressed cohesionless soils
S	Base length of the slice
S_m	the shear force on the base of the slice
u	pore water pressure
$X_R - X_L$	vertical interslice forces acting on the right and left sides of the slice, respectively
W	weight of the slice
W	weight of the soil mass on the failure surface
y_n	Length of the left side of the n^{th} slice
y_{n+1}	Length of the right side of the n^{th} slice

α_ψ, m_ψ	unit-independent fitting parameters which vary with relative density index
β	the slope angle of the base of the slice
$\varepsilon_s, \varepsilon_y$	linear strains in the x and y directions respectively
δ	the friction angle between the backfill and the wall
θ	angle of the resultant interslice force measured from the horizontal
λ	a constant to be evaluated in describing the directions of interslice forces
σ_h	effective horizontal stress
σ_v	effective vertical stress
ϕ'	effective internal friction angle
ψ_p	peak dilatancy angle
p_i	pre-shear mean effective stress standard atmospheric pressure at sea level
γ	Unit weight of backfill
γ	maximum shear strain
γ_{xy}	the shear strain in the x-y plane
Δl	length of the base of the slice
ϕ_p	peak friction angle
l_σ	locked-in stress at base of a slice

LIST OF ACRONYMS/ABBREVIATIONS

ASTM	American society for testing and materials
ASCE	American Society of Civil Engineering
PIV	Particle image velocimetry method

1. INTRODUCTION

1.1. Theory Background

The aim of this thesis is to determine effects of the dilatancy angle of cohesionless soil on the lateral earth forces acting on the retaining walls. Correct calculation of the lateral earth forces that soil backfills exert on geotechnical structures, such as piles and retaining walls should be regarded during design of these structures. Soil parameters play a critical role towards correct determination of these forces. According the soil plasticity theory, one of these important parameters is dilatancy angle.

For this purpose, a new method was developed by modifying the methods of slices proposed in the previous studies (Janbu, 1957; Morgenstern and Price, 1965; Shields and Tolunay, 1973; Fan, 1983; Rahardjo and Fredlund, 1984). Within this method, the equation based on dilatancy angle to identify active failure surface geometries proposed by Altunbaş (2014) was used to decide on the failure surface geometries for soil backfills at different relative densities. Accuracy of the developed method was evaluated through small scale retaining wall model tests. In these tests, backfill at different relative densities were tested to active failure using a horizontally translating small scale retaining wall model. Backfill dilatancy and friction angles are calculated using the equations proposed by Çinicioğlu and Abadkon (2014). Active thrust on the model wall is obtained through the pressure transducers mounted on the model wall. Measured thrust is compared with the calculated thrust using the proposed equation based on the calculated dilatancy angles. Additionally, results were compared with the popular methods of calculating the active thrust, namely Coloumb (1776) and Rankine (1857) theories.

2. LITERATURE REVIEW

2.1. Active Earth Pressure

Determination of the active lateral earth pressure has a huge effect on the design of many geotechnical structures such as, highway, tunnel, mining, and retaining walls. Coloumb's (1776) and Rankine's (1857) theories are mostly used for calculation of the active earth pressure. According to these theories, the distribution of active earth pressure acting on the retaining wall is triangular Figure 2.1 and Figure 2.2 show the distribution of the active earth pressure on the wall regarding to Coloumb and Rankine theories, respectively.

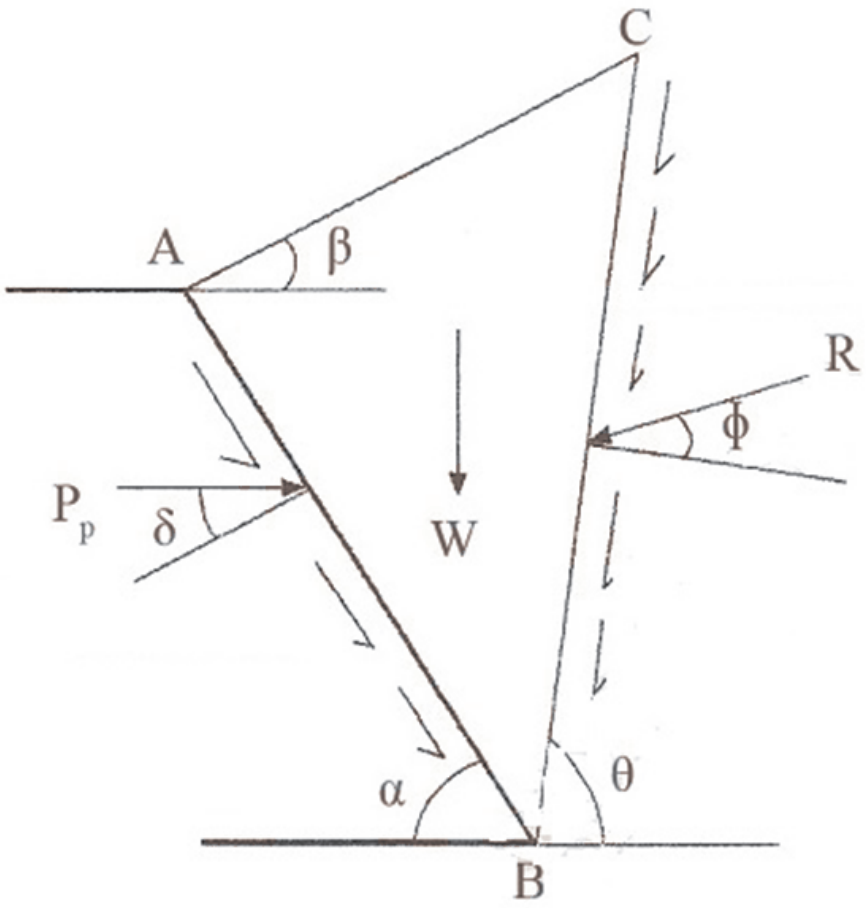


Figure 2.1. Coloumb theory for Active Earth Pressure.

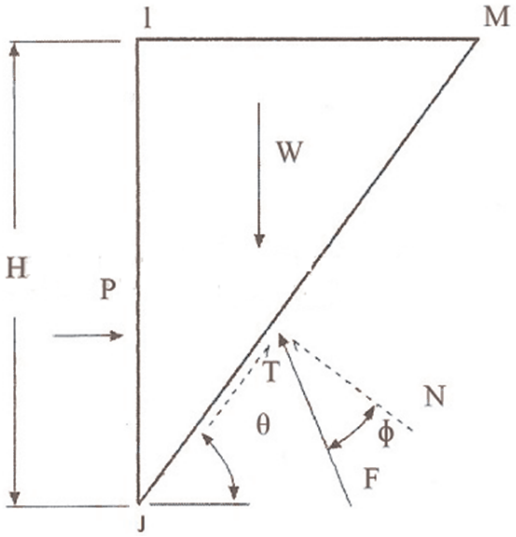


Figure 2.2. Rankine theory for Active Earth Pressure.

Besides, the results of the experiments conducted to investigate active earth pressures are shown that the active earth pressure distribution acting on a retaining wall is nonlinear by contrast with the theories of Coloumb and Rankine. Another shortcoming of such theories is underestimation of the height of the center of pressure. Some investigations have been conducted to find out the underlying reasons of this nonlinearity. These studies are based on the shape of slip surface, magnitude and height of application of lateral active force in retained soil mass.

Terzaghi (1936) investigated the effect of the wall movement on lateral earth pressures from at-rest to active or passive state. He argued that arching effect led the failure surface to be approximately parabolic. Arching is the stress redistribution process by which stress is transferred around a region of soil mass, which as a result reduces the stresses on the soil mass (Goel and Patra, 2008). A simple example of arching is what occurs in a large box of soil with a panel at the base. When this panel is lowered, the soil immediately above it will tend to move down with it as can be seen in Figure 2.3.

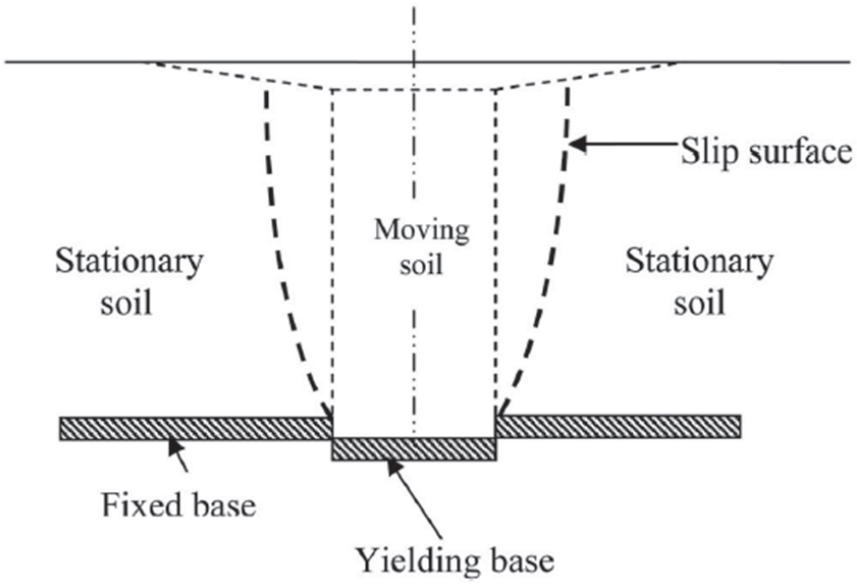


Figure 2.3. Stress Redistribution Caused by Arching (Paik and Salgado, 2003).

Handy (1985) studied soil arching. He depicted soil arching action as a trajectory of minor principle stress that approximates a catenary. According to Handy, soil arching occurs in two stages. First of these stages is rotation of principal stresses at the wall. This rotation brings about earth pressures higher than that Rankine and Coloumb theories assume. At its maximum development, it approximately equals the Jaky expression for earth pressure at rest. As the wall moves, a semi-arch between the wall and the failure surface forms. This second stage of arching reduces vertical and horizontal pressures, particularly near the base of the wall. It yields a rounded pressure distribution rather than triangular pressure distribution, with the center of action about 0. 4 - 0. 45 times the height of the wall. In its second stage, arching action reduces wall pressures significantly below those from the Coulomb analysis, but places their center of action higher on the wall; the two effects are approximately compensatory for determining overturning moments. The curved pressure distribution from arching theory is relevant for calculation of shear and bending moments at various levels in the wall (Handy, 1985).

Paik and Salgado (2003) investigated the arching effects on the calculation of active earth pressure on the wall. They suggested a new formulation that includes

both the earth pressure distribution and the lateral active force on the translating wall. According to Paik and Salgado, the shape of the failure surface depends on both wall friction angle and the yielding mode. In their study, Janssen (1895) arching theory was utilized for investigation of the state of stress in the soil backfill. Regarding to their investigation, the assumption that two parallel rigid vertical walls retain granular soil is accepted. The second assumption of Paik and Salgado is that the settlement of the retained soil is large enough to completely generate friction between the wall and the soil. As a result, the weight of any differential element in the soil is partly supported by the frictional resistances at the walls. These resistances induce changes in the direction of the principle stresses acting on the element. These changes are shown in Figure 2.4.

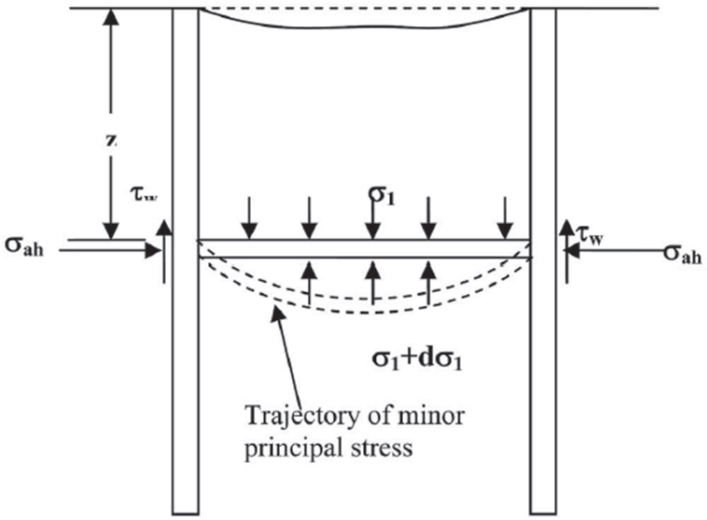


Figure 2.4. Trajectory of Minor Principal Stresses in Granular fill at Ditch (Paik and Salgado, 2003).

The major principal stresses on the element are normal stresses. These stresses are applied to the concave arch. The minor principle stresses are tangent to the direction of the concave arch. The direction of the major and minor principal stresses on the differential flat element, induced in the case that a rigid retaining wall with a rough face horizontally moves away from the soil, is shown in Figure 2.5.

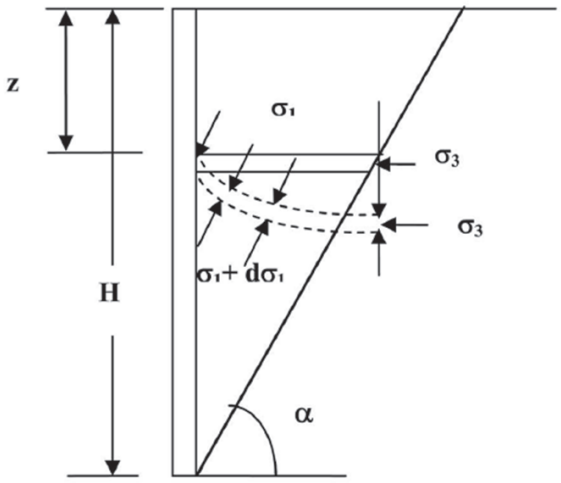


Figure 2.5. Trajectory of Minor Principal Stresses in Backfill Behind Retaining Wall (Paik and Salgado, 2003).

The minor principal stresses on the differential flat element behind the wall acted along the concave arch are shown in Figure 2.5. Major principal stresses perpendicularly act on the concave arch. Paik and Salgado (2003) obtained the rotation angle of the principle stresses for the wall with a wall friction angle smaller than the rotation angle of the principal stresses by utilizing the Mohr circle as shown in Figure 2.6.

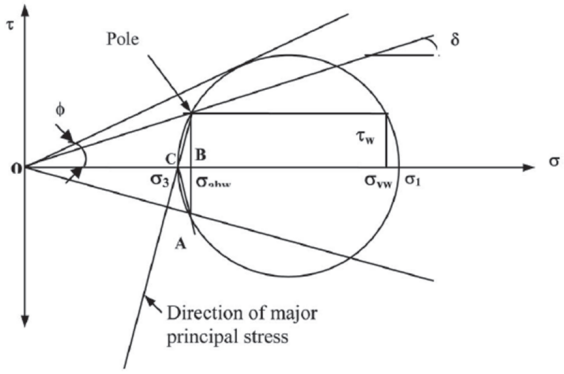


Figure 2.6. Mohr Circle for Stresses at Wall (Paik and Salgado, 2003).

Paik and Salgado (2003) investigated the effects of frictional angle, soil-wall interface friction angle and the height of the wall by conducting a parametric study. As a result of their study, they obtained that an increase in the internal friction angle results in a decrease in the active earth pressure distribution acting on the wall at every

depth. They also showed that an increase in soil-wall interface friction angle causes an increase in the height of the centroid of the active earth pressure distribution and the distance of the centroid of the active earth pressure distribution from the base of the wall.

Paik and Salgado (2003) also suggested that although shape of the active earth pressure distribution is not influenced by the wall height, the magnitude of the lateral active force depends on the wall height. As a result, they proposed that the ratio of the height of the point of application of the lateral active force to the wall height is independent of wall height for all formulations.

Goel and Patra (2008) investigated the influences of the arching effects and the shape of the critical failure surface on active earth pressure distribution for rigid retaining walls. To investigate these effects, they used various shapes for the critical failure surface and the arching mechanism. These are planar failure surfaces with a parabolic arch and parabolic failure surfaces with a parabolic arch. Based on their results, they claimed that planar failure surface with parabolic arch shape predicts closest to the experimental values.

2.2. Small Scale Retaining Wall Model

Hanna and Khoury (2005) performed an experimental investigation into the coefficient of passive earth pressure of overcomplicated homogeneous sand. They used a prototype model of a vertical rough wall model for their investigation as shown in Figure 2.7. The model was instrumented to measure the total passive earth pressure acting on the wall.

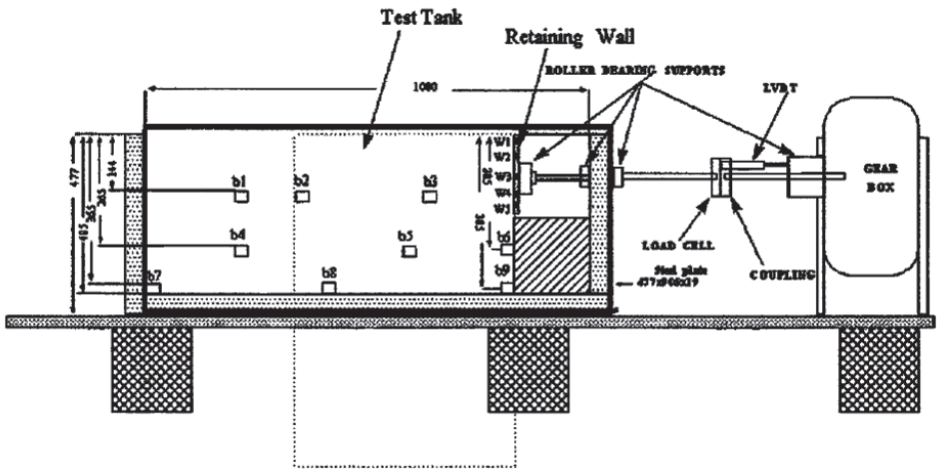


Figure 2.7. Layout of Experimental Setup (Hanna and Khoury (2005).

In the retaining wall model designed by Hanna and Khoury (2005), the side of the testing tank are plexiglass to allow observation of the sand deformation during testing. The loading system consisted of a gearbox capable of producing a wide range of strain rates. A metal plate was used to simulate the retaining wall. The rod was connected to the loading system through a load cell to measure the horizontal component of the total passive earth pressure acting on the wall. In order to measure the distribution of the passive earth pressure acting on the wall, five pressure transducers were mounted on the plate, which simulates the wall, shown in Figure 2.8.

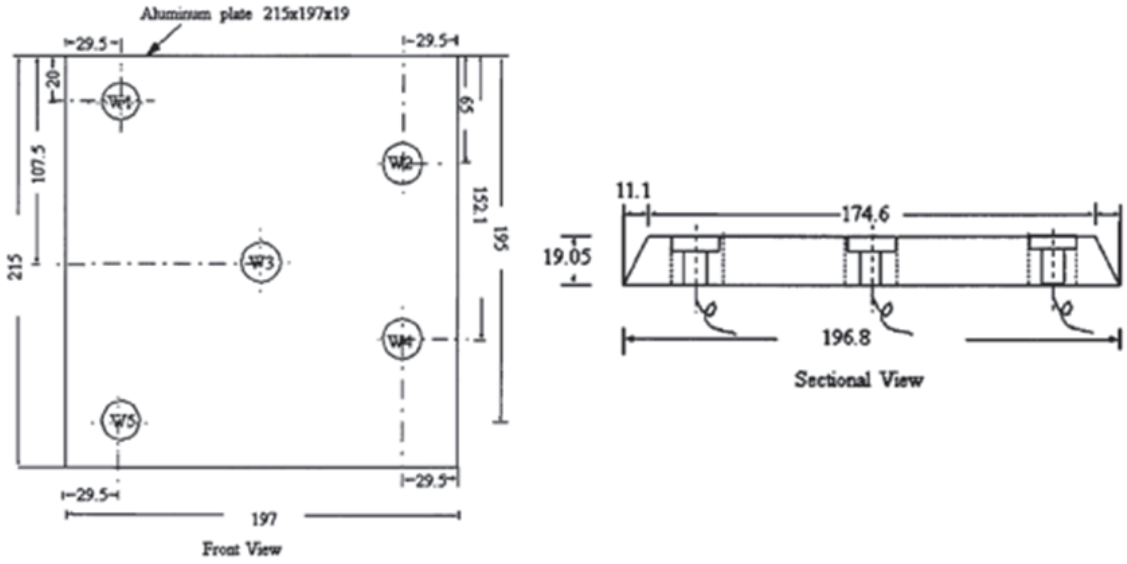


Figure 2.8. Location of Transducers on Retaining Wall (Hanna and Khoury 2005).

The induced vertical stresses in the sand mass due to compaction were measured by means of nine pressure transducer units shown in Figure 2.7. They are placed in the sand mass at three levels. Each unit was housed in a metal box made of aluminium connected to a hollow bar, through which the electrical wires pass to the data acquisition system. The scheme of the box is shown in Figure 2.9.

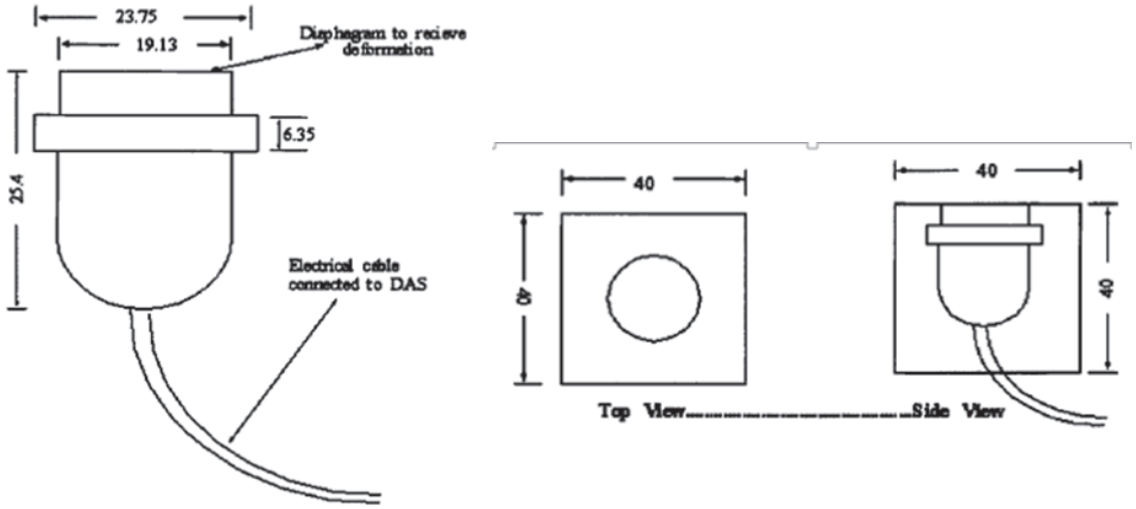


Figure 2.9. Transducers Box Unit Used to Measure Vertical Stresses in Sand Mass (Hanna and Khoury (2005).

Hanna and Khoury (2005) used density cans to measure the unit weight of the sand in the testing tank. These cans were placed in a staggered scheme in the vertical direction to avoid boundary effects. At the end of each test, these cans were carefully taken out and weighed. By using the weight of the cans, the unit weight of the sand was taken as the average unit weight of the sand in these cans to calculate the relative density according to ASTM D-2049. To obtain the desired unit weight, they spread the sand through a hose from a minimal height to minimize particle segregation. In cases when the desired unit weight is high, they applied compaction to each layer using a hand air compactor with an end steel plate. The air pressure of the compactor was fixed to a value of 207 kPa and the range of the compaction duration varied from 2 to 11 s. The relationship between the compaction duration and the mechanical properties of the sand was established in the laboratory before testing.

2.3. Dilatancy Angle and Peak Friction Angle of Cohesionless Soils

Çinicioğlu and Abadkon (2014) established a relationship between dilatancy angle, pre-shear mean effective stress and relative density for cohesionless soils. They aimed to determine dilatancy angle at exploration phase of a design project. In accordance with their objective, an experimental study regarding triaxial tests on local Standard Ottawa sand was conducted. In addition to this, they examined the data of the study conducted by Vaid and Sasitharan (1992) on Erksak sand. As a result of conducted experiments and examination of the previous studies, they proposed the formula shown in Equation 2.1 to determine dilatancy angle in terms of two unit independent soil constants.

$$\tan \psi_p = \alpha_\psi \left(\frac{p'_i}{p_a} \right) + m_\psi I_D \tag{2.1}$$

where is the α_ψ and m_ψ unit-independent fitting parameters which vary with relative density index $I_\psi 00$. ψ_p peak dilatancy angle p_i for pre-shear mean effective stress standard atmospheric pressure at sea level.

α_ψ corresponds to the decrease in dilatancy angle per unit increase in normalized confinement whereas m_ψ corresponds to the increase in dilatancy angle per unit increase in relative density.

In addition, Çinicioğlu and Abadkon (2014) also quantified peak friction angle of cohesionless soils as functions of pre-shearing relative density and mean effective stress. To define peak friction angle, they needed two more parameters except α_ψ and m_ψ require to calculate dilatancy angle in Equation 2.1. These parameters are r and ϕ'_c r is a line-fitting parameter and ϕ'_c is residual friction angle obtained from the tests conducted in direct shear and triaxial apparatuses. The equation that gives peak friction angle is shown in Equation 2.2 (Çinicioğlu and Abadkon (2014).

$$\phi'_p = \phi'_c + r \left[\tan^{-1} \left(\alpha_\psi \left(\frac{p'_i}{p_a} \right) + m_\psi I_D \right) \right] \tag{2.2}$$

where is the ϕ'_p peak friction angle.

2.4. Method of Slices

In method of slices, which is used in slope stability problems, the normal force acting on the base of each slice is described to calculate factor of safety (FS). In this section, it is considered how the normal forces are described in the previous theories about method of slices.

2.5. Ordinary Method of Slices

The Ordinary Method of Slices is named as the "Fellenius Method". This method was proposed by Fellenius (1936). The ordinary method of slices is considered the simplest methods of slices because it provides a linear factor of safety equation. It neglects the interslice forces on the sides of the slice as shown in Figure 2.10. The reason for such negligence is that the interslice forces are parallel to the base of each slice.

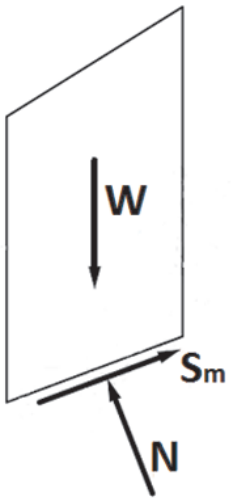


Figure 2.10. Slices with Forces Considered in the Ordinary Method of Slice.

However, Newton's principle is that action equal to reaction is not satisfied between slices in this method. Two slices are shown in Figure 2.11 Q_{R5} is not equal and opposite to Q_{L6}. Because of the indiscriminate change in direction of the resultant

interslice force from one slice to the next, the method is not safe.

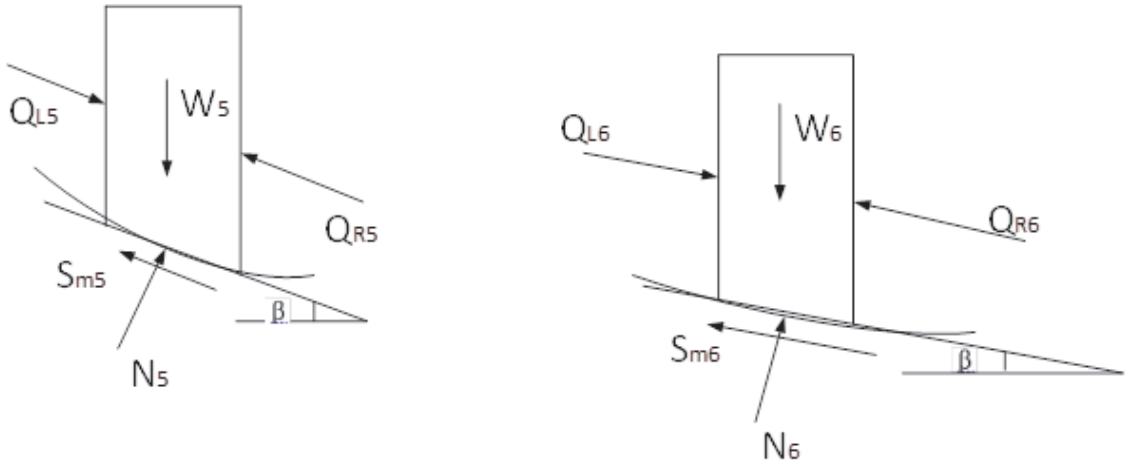


Figure 2.11. Forces Actually Actingon the Slice in the Ordinary Method of Slice.

The normal force on the base of each slice is derived from the summation of forces in the vertical and horizontal directions.
For equilibrium of the forces in vertical direction:

$$W - N \times \cos\beta - S_m \times \sin\beta = 0 \tag{2.3}$$

where is the S_m shear force, is the N normal force, is the β slope angle of the base of the slice, is the W weight of the slice. For equilibrium of the forces in horizontal direction:

$$S_m \times \cos\beta - N \times \sin\beta = 0 \tag{2.4}$$

Combining Equation 2.3 and Equation 2.4, and solving for the normal force gives

$$N = W \times \cos\beta \tag{2.5}$$

2.5.1. Simplified Bishop Method

According to Simplified Bishop method (1955), the interslice forces are assumed to be horizontal. In other words, there are no interslice shear forces between the slices. The forces acting on the slice based on "Simplified Bishop Method" are shown in Figure 2.12.

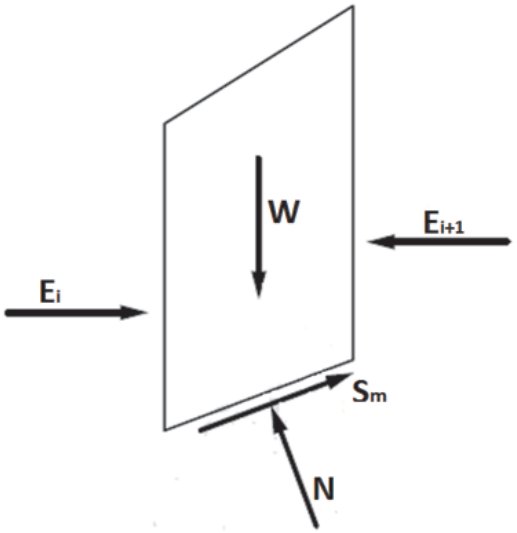


Figure 2.12. Slices with Forces Considered in Simplified Bishop Method.

For equilibrium of the forces in vertical direction:

$$W - N \times \cos\beta - S_m \times \sin\beta = 0 \tag{2.6}$$

The normal force on the base of each slice is derived by summing forces in a vertical direction.

$$N = \frac{W - S_m \times \sin\beta}{\cos\beta} \tag{2.7}$$

By identifying the shear force (S_m) in terms of normal force as indicated in the Mohr-Coloumb strength equation, the normal force can be described.

$$N = \frac{W - (1/F) \times (c' \times \Delta l - u \times \Delta l \times \tan\phi') \times \sin\beta}{\cos\beta + (\sin\beta \times \tan\phi')/F} \tag{2.8}$$

where is the F factor of safety, is the c' effective cohesion, is the Δl length of the base of the slice, is the U pore water pressure, is the ϕ' effective internal friction angle.

2.5.2. Spencer's Method

According to Spencer's method (1967), there is a constant relationship between the magnitude of the interslice shear and normal forces as given by the expression below:

$$\tan\theta = \frac{X_L}{E_L} = \frac{X_R}{E_R} \tag{2.9}$$

where is the θ angle of the resultant interslice force measured from the horizontal.

The interslice forces and other forces acting on the slice are shown in Figure 2.13.

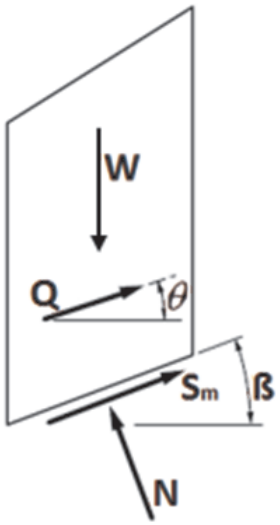


Figure 2.13. Slices with Forces Considered in Spencer's Method.

According to Spencer's method, equilibrium of the forces acting on the slice can be obtained in two ways. First method requires the summation of forces that are perpendicular to interslice forces. The second method requires the summation of forces in vertical and horizontal directions. The answers for the normal force are the same in both two ways.

For equilibrium of forces in vertical direction:

$$W - (X_R - X_L) - N \times \cos\beta - S_m \times \sin\beta = 0 \tag{2.10}$$

where is the X_R and X_L vertical interslice forces acting on the right and left sides of the slice, respectively.
For equilibrium of the forces in horizontal direction:

$$N \times \sin\beta - (E_R - E_L) - S_m \times \cos\beta + kW = 0 \tag{2.11}$$

where is the k seismic coefficient to account for a dynamic horizontal force, is the E_R and E_L horizontal interslice forces acting on the right and left sides of the slice, respectively.
Normal force can be derived from force equilibrium in vertical direction:

$$N = \left[\frac{W - (E_R - E_L) \times \tan\theta - \frac{c' \times l \times \sin\beta}{F} + \frac{u \times l \times \tan\phi' \times \sin\beta}{F}}{\frac{\cos\beta + (\sin\beta \times \tan\phi')}{F}} \right] \tag{2.12}$$

The difference between horizontal interslice forces on the right and left sides of the slice is described from the force equilibrium in horizontal direction:

$$(E_R - E_L) = N \times \sin\beta - S_m \times \cos\beta + kW \tag{2.13}$$

2.5.3. Janbu's Simplified Method

The Simplified Janbu procedure (1956) is based on the assumption that the interslice forces are horizontal. This method is similar to "Simplified Bishop Method" in the way the normal force acting on the base of the slice is computed.

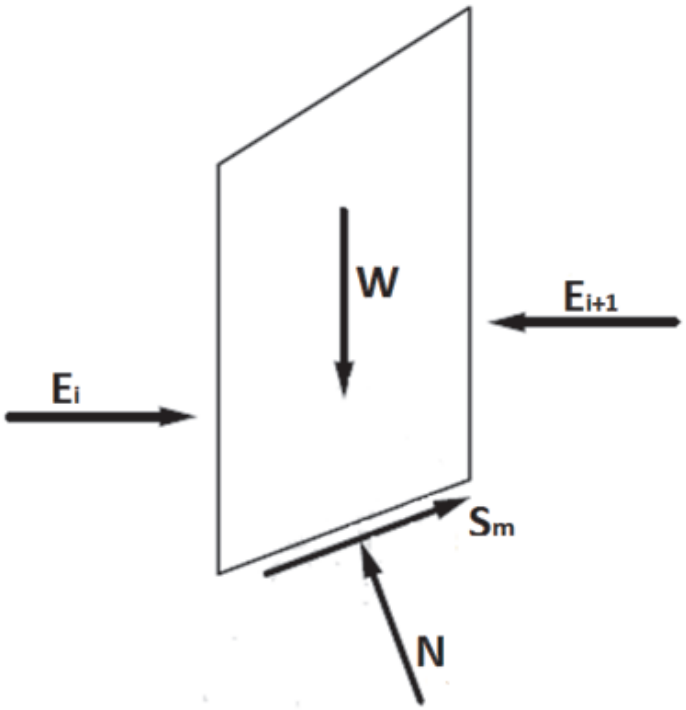


Figure 2.14. Slices with Forces Considered in Simplified Janbu Method.

The normal force acting on the base of the slice is derived from the equilibrium of vertical forces as the interslice shear forces are ignored:

$$N = \left[\frac{W - \frac{c' \times l \times \sin\beta}{F} + \frac{u \times l \times \tan\phi' \times \sin\beta}{F}}{\frac{\cos\beta + (\sin\beta \times \tan\phi')}{F}} \right] \tag{2.14}$$

2.5.4. Janbu's Rigorous Method

In this method, the point at which the interslice forces act is defined by a "line of thrust". The forces acting on the slice according to "Janbu's Rigorous method" are shown in Figure 2.15.

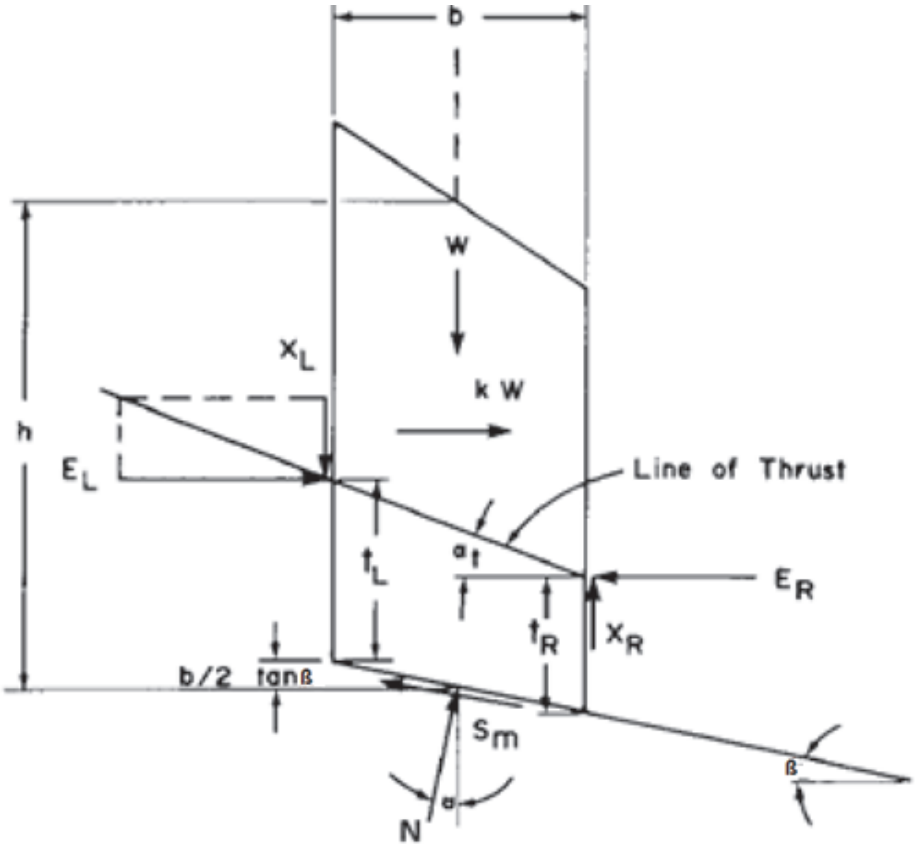


Figure 2.15. Slices with Forces Considered in Janbu's Rigorous Method.

In Figure 2.15, t_R and t_L are vertical distances from the base of the slice to the line of thrust on the right and left sides of the slice, respectively; α_t is angle between the line of thrust on the right side of a slice and the horizontal.
The normal force on the base of the slice is derived from the summation of vertical forces.

$$N = \left[\frac{W - (X_R - X_L) - \frac{c' \times l \times \sin\beta}{F} + \frac{u \times l \times \tan\phi' \times \sin\beta}{F}}{\frac{\cos\beta + (\sin\beta \times \tan\phi')}{F}} \right] \tag{2.15}$$

To compute the normal force acting on the base of the slice, the interslice shear forces must be evaluated. For the evaluation of the interslice shear forces, some iterations are utilized. Firstly, the shear forces are set to zero. For subsequent iterations, interslice forces are calculated by using moment equilibrium about the center of the

base of a slice.

$$\begin{aligned}\textstyle\sum M_c &= X_L \times \tfrac{b}{2} + X_R \times \tfrac{b}{2} - E_L \times \left[t_L + \tan\beta \times \tfrac{b}{2}\right] \\ &+ E_R \times \left[t_L + \tan\beta \times \tfrac{b}{2} - b \times \tan\alpha_t\right] - \tfrac{k \times W \times h}{2} = 0\end{aligned} \tag{2.16}$$

In Equation 2.16, some terms become negligible because the width of the slice (b) is reduced to a width (dx). Using the reduction of the width of the slice, the interslice shear force on the right side of a slice can be identified.

$$X_R = E_R \tan\alpha_t - (E_R - E_L) \times t_R/b + (kW/b) \times (h/2) \tag{2.17}$$

Interslice normal forces that are required for the solution of interslice shear forces on the right side of the slices are obtained by using the force equilibrium in vertical and horizontal directions for each slice.

$$(E_R - E_L) = [W - (X_R - X_L)] \times \tan\beta - S_m/\cos\beta + kW \tag{2.18}$$

Interslice normal forces are described by integrating from left to right across the slope. The magnitude of the interslice shear forces in Equation 2.18 lag by one iteration. Each iteration gives a new set of shear forces. The vertical and horizontal components of line loads must also be taken into account when they are encountered.

2.5.5. Morgenstern-Price Method)

While using the Morgenstern-Price method (1965), an arbitrary mathematical function is assumed to determine the directions of interslice forces.

$$\lambda \times f(x) = X/E \tag{2.19}$$

where is the λ a constant to be evaluated in describing the directions of interslice forces, is the $f(x)$ functional variation respect to x, horizontal distance from the slice to the center of rotation.

In this method, various types of functions can be utilized. Figure 2.16 shows typical functions.

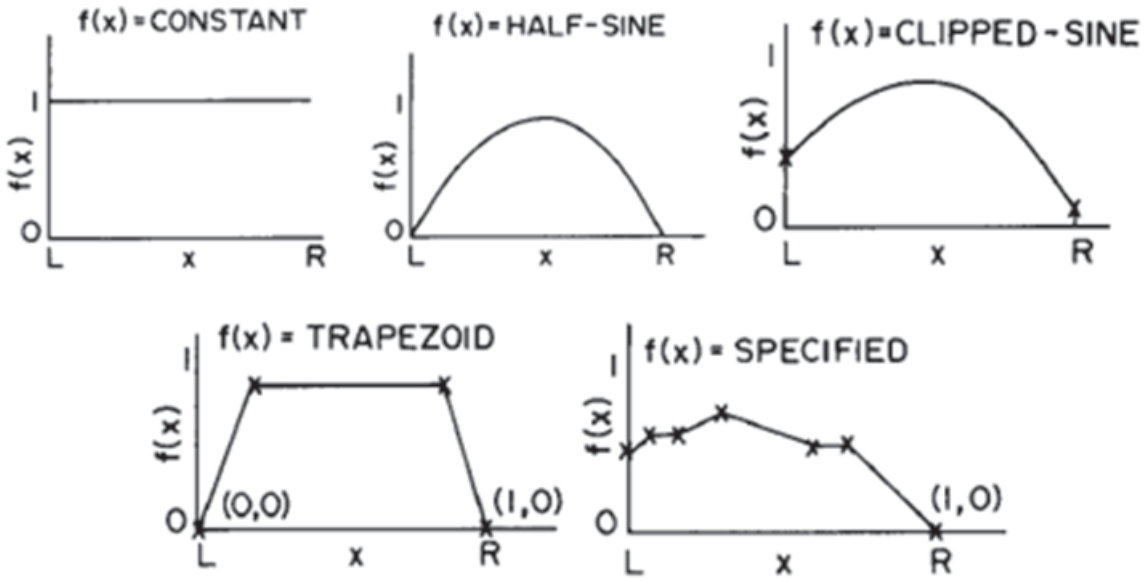


Figure 2.16. Functional Variation of the Direction of the Side Force with Respect to the x Direction.

The normal force acting on the base of a slice is derived from the force equilibrium in vertical direction. The formula derived to describe the normal force is the same as the equation used in Janbu's Rigorous method.

$$N = \left[\frac{W - (X_R - X_L) - \frac{c' \times l \times \sin\beta}{F} + \frac{u \times l \times \tan\phi' \times \sin\beta}{F}}{\frac{\cos\beta + (\sin\beta \times \tan\phi')}{F}} \right] \tag{2.20}$$

In Morgenstern-Price method, a method similar to Janbu's rigorous method is used to calculate the interslice shear forces. On the first iteration, the vertical shear forces are set to zero. Then, the horizontal interslice forces are computed using Equation 2.18. After computation, the vertical shear forces are calculated by using an

assumed λ value and the interslice force function as shown in Equation 2.21. Finally, side forces are recomputed for each iteration.

$$X_R = E_R \times \lambda \times f(x) \tag{2.21}$$

2.6. General Limit Equilibrium Methods for the computation of Lateral Earth Thrust

The limit equilibrium method of slices has been widely used for the analysis of slope stability problems. The principles of limit equilibrium used for analyzing slope stability can also be used to analyze lateral earth force problems.

Janbu (1957) proposed to solve lateral earth force problems by using the generalized procedure of slices and a composite slip surface. The active and passive earth pressures were calculated for dry sand. Shields and Tolunay (1972) calculated the passive earth pressure coefficients, K_p, by utilizing logarithmic spiral method suggested by Terzaghi and Peck (1967). They used dry, cohesionless sand with a horizontal surface behind a vertical, rough wall during their study.

Shields and Tolunay (1973) have computed the values for passive earth pressure coefficient, K_p, based on method of slices and a composite slip surface. The values for passive earth pressure coefficient, K_p, obtained using the method of slices were slightly lower than the values previously computed with the logarithmic spiral method (i. e. , an average of 4. 5% lower for values of wall friction angle d ranging between 0 and 20°).

Fredlund *et al.*, (1981) suggested the solution of slope stability problems using general limit equilibrium (GLE) method of slices approach. Rahardjo (1982) improved the GLE formulation to lateral earth pressure problems. In addition to this, Rahardja (1982) showed the influence of the interslice force function on the values of the lateral force and the point of application. Fan (1983) used the finite element stress analyses

with a linear elastic soil model to compute an approximate function for the direction of the resultant interslice forces associated with the active and the passive cases.

Rahardjo and Fredlund (1984) illustrated the influence of a variety of possible interslice force functions on the magnitude of the lateral earth force. Figure 2.17 shows three types of interslice force functions. The functions used for active cases and the functions used for the passive cases are shown in Figure 2.17, respectively. (Rahardjo and Fredlund, 1984).

Chen and Li (1998) also calculated the magnitude of the active force by using method of slices. They assumed different slip surfaces. In addition, Chen and Li took the slip surface associated with the maximum active force to be the critical slip surface. The point of application of the active force was assumed and the magnitude of the active earth force satisfying force and moment equilibrium was calculated. The magnitude of the active force was computed for various assumptions for the point of application. The effect of wall friction angle was not considered.

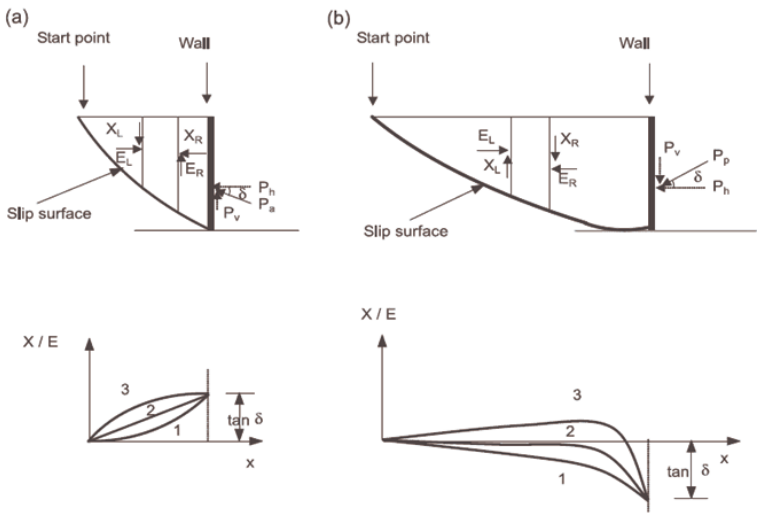


Figure 2.17. Possible Interslice Force Functions for a Horizontal Backslope: (i) Active Case, (ii) Passive Case (From Rahardjo and Fredlund 1984).

3. TESTING METHODOLOGY

3.1. Properties of the Small Scale Retaining Wall Model

The physical model consists of a testing tank, a movable model retaining wall, a sand pluviation system, storage tank, crane and multi-channel data logger (Figure 3.11).

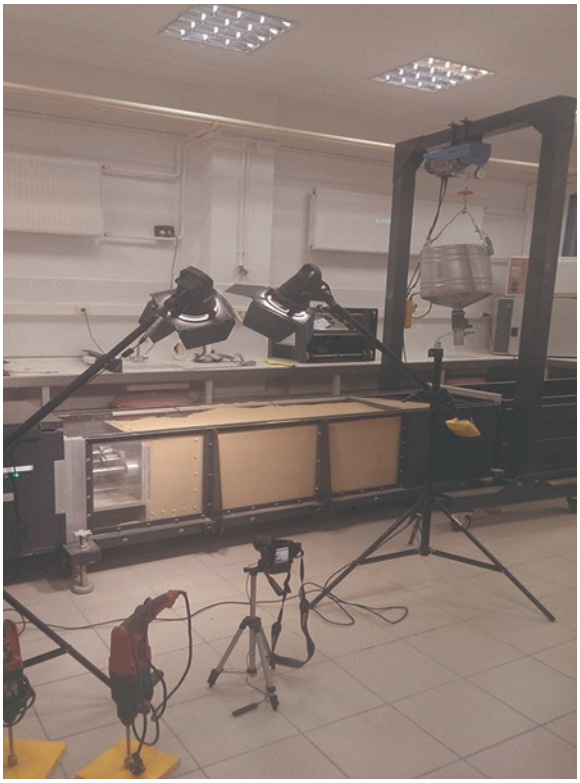


Figure 3.1. Experimental Set-Up.

The sides of the testing tank are 50 mm thick plexiglass allowing the observation and photographing of the deformations during testing. The testing tank is 140, 60, and 50 cm in length, width and depth, respectively. The dimensions are shown in Figure 3.2.

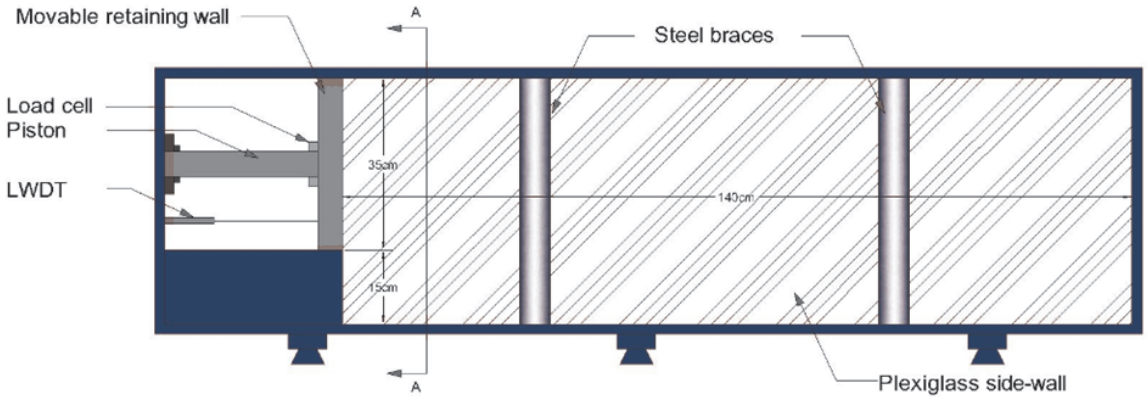


Figure 3.2. Crossectional view of the Physical Model.

An aluminium plate capable of lateral translation acts as the retaining wall. The plate has a rectangular cross-section 35 cm high and 50 cm wide. The plate is placed 15 cm above the base of the test tank to minimize the negative effects of the rigid boundary at the bottom. It can move either in forward or backward directions. The horizontal movement of the wall is provided by an electrical motor. There are five sensitive pressure transducers mounted on the retaining wall model at equally spaced intervals. These transducers, that have the capacity of 200 kPa, allow the measurement of lateral earth pressures acting on the model wall. Front view of the model wall is depicted in Figure 3.3. In addition to these, two transducers are buried in the backfill during the model preparation to measure the the vertical earth pressures.

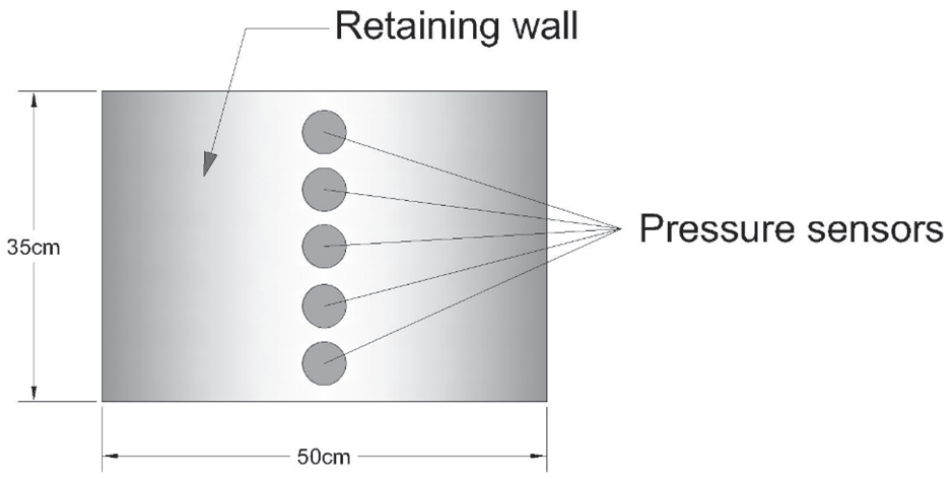


Figure 3.3. The Location of Pressure Transducers and Transparent Side Walls.

The load cell, which has 5kN capacity, is used to measure the magnitude of the lateral thrust required for the translation of the plate. There is also an electric ruler at the same location to measure the displacement of the wall. The load cell and the eclectic ruler in the system are shown in Figure 3.4.

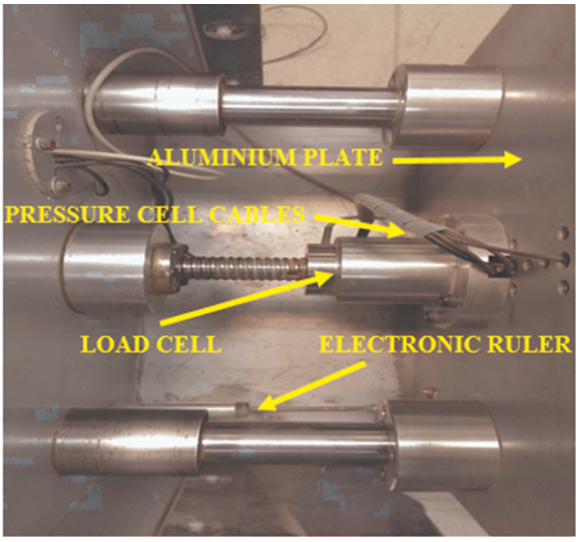


Figure 3.4. The Back Face of the Retaining Wall.

The mobile crane is used to transfer the sand between the test tank and the storage tank. A multi-channel data logger system is used to collect data. This system has eight channels, and it is capable of sensitively recording the readings coming from the measuring devices in an automatic mode at predetermined intervals (Figure 3.5).



Figure 3.5. The Data Acquisition System.

3.2. Properties of the Testing Sand

The soil used in the present study is Akpinar sand. Akpinar sand was washed, dried and then sieved. The grain size distribution of Akpinar Sand is shown in Figure 3.6. By using the gradation curve, uniformity and curvature coefficients of the sand were obtained. Based on the coefficient values, the sand is classified as poorly graded sand (SP).

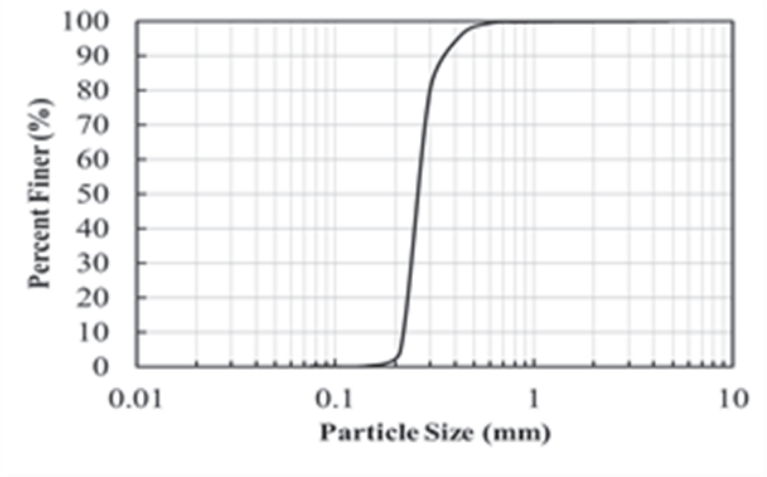


Figure 3.6. Sieve Analysis of Tested Sand.

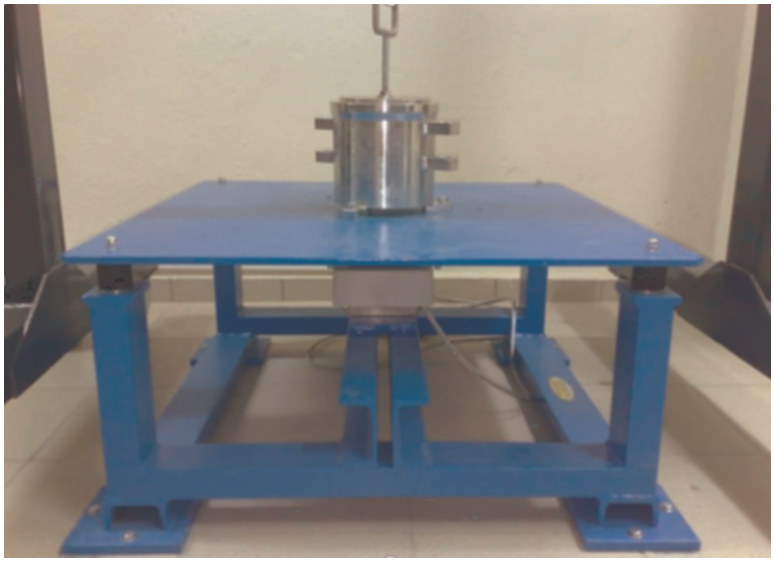


Figure 3.7. Vibratory Table Used to Determine Maximum Minimum Void Ratios.

In order to obtain maximum and minimum void ratios of the testing sand, relative

density tests on the vibratory table (Figure 3.7) were conducted in accordance with the related standards (ASTM D-4253 and ASTM D-4254).

The properties of Akpinar sand are shown in Table 3.1.

Table 3.1. The Properties of Tested Sand.

Property	Value
Classification	Poorly Graded (SP)
Max. void ratio (e_{max})	0.87 (ASTM)
Min. void ratio (e_{min})	0.58 (ASTM)
Uniformity coefficient (C_u)	1.23
Coefficient of gradation (C_c)	0.97
Specific gravity (G_s)	2.63
Average sphericity, S_{ave}	0.7
Average roundness, R_{ave}	0.5
Wall-backfill interface friction $\delta(^o)$	19
Plexiglass-backfill interface friction $\delta(^o)$	17
Critical state friction angle $\phi'(^o)$	33
Line-fitting parameter (r)	0.39
Stress-based dilatancy canstant (α_ψ)	-0.066
Density-based dilatancy canstant (m_ψ)	0.64

3.3. Direct Shear Test

Within this study, the interface friction angle between the model retaining wall and the sand backfill and the interface friction angle between the plexiglass and the sand backfill must be determined to be used in the calculations. To determine such interface friction angle values, several direct shear tests were conducted. For these tests, samples of the retaining wall and Plexiglas wall are made out of the same materials. The samples have dimensions of 10 cm x 10 cm. These samples are shown in Figure 3.8.

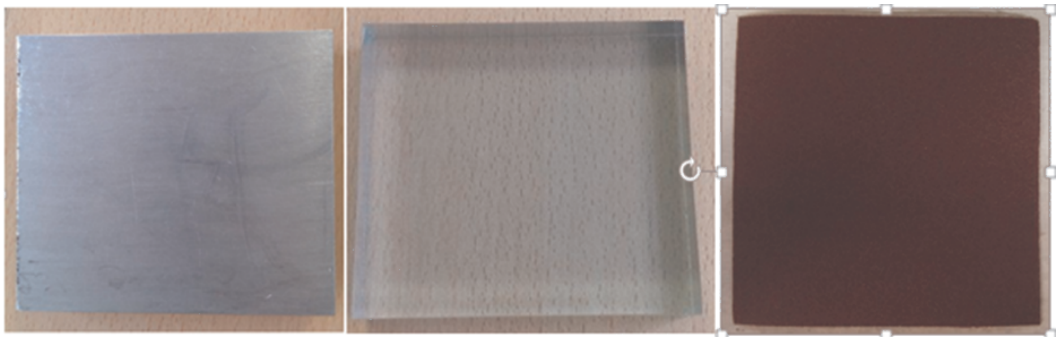


Figure 3.8. The Samples of (i) The Model Retaining Wall, (ii) The Plexiglass, and (iii) The Sand Paper.

3.3.1. Test Procedure

The laboratory book of Bardet (1997), Experimental Soil Mechanics is utilized as a main reference in this section.

(i) The internal side length for square cell was measured.

(ii) The counterweight system calibrated so that it applies a small but negligible normal force.

(iii)I The cap was weighted.

(i) The direct shear box assembled and mounted it on the direct shear machine. The mounting pins were inserted to align the upper and lower parts of the direct shear box.

(iv) The gap between the two parts of the shear box adjusted by turning the setscrews. In theory, the spacing should be larger than the diameter of the largest particle to prevent the top part from riding up on the grains that get caught in the gap. In practice, a spacing of approximately 0. 5 mm is satisfactory.

(v) The depth H2 of the shear box and the height H3 of the top cap were measured.

(vi) The dish filled with the sand to be tested was weighted.

(vii)I The interface material is placed into lower part of the direct shear box.

(viii) While the pins hold the two parts of the shear box together, the sand was placed into upper part of the direct shear box by pouring method (Figure 3.9). To prepare loose specimen, the sand was poured slowly to obtain a loose specimen.

The sand was compacted with a tamper to obtain denser specimens.

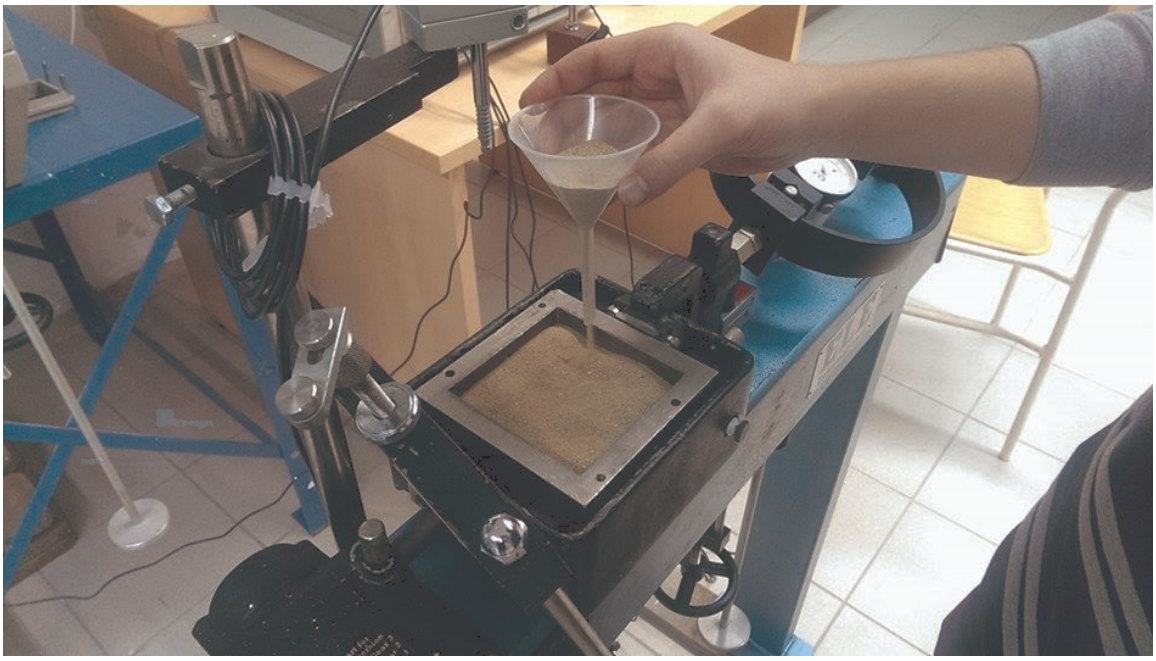
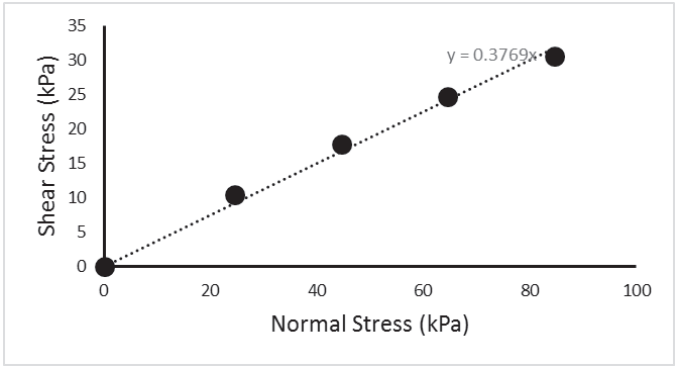


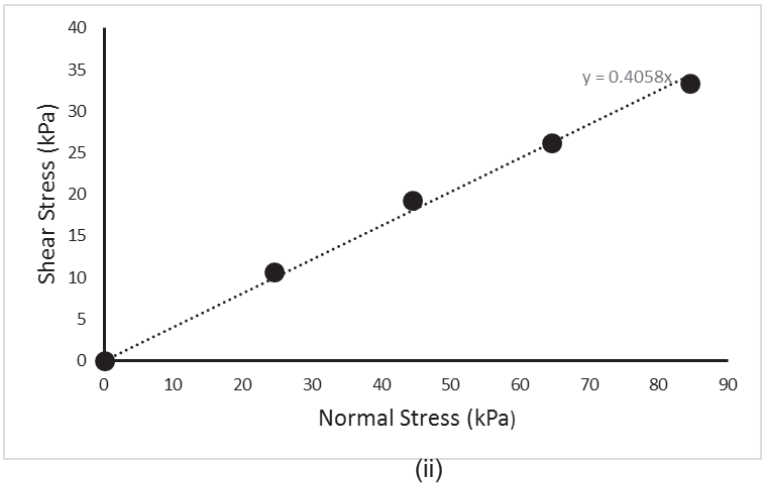
Figure 3.9. Preparation of Direct Shear Test.

3.4. Data Analysis

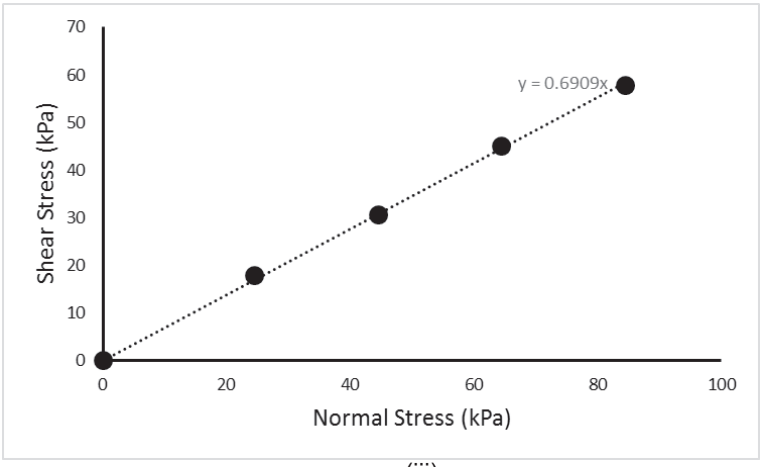
For determination of the friction angle for the sand-model wall, sand-side wall, sand-wall covered with sand paper interfaces direct shear tests were conducted. The reason for using sand paper is to create and abrasive surface which has different frictional property than the model wall surface. Four tests were conducted for each interface. In other words, totaly sixteen direct shear tests are conducted. The results obtained are shown in Figure 3.10.



(i)



(ii)



(iii)

Figure 3.10. Direct Shear Test Results for (i) The Wall Model-Backfill Interface, (ii) Plexiglass-Backfill Interface and (iii) Sandpaper-Backfill Interface.

3.5. Placement of the Backfill in the Small Scale Retaining Wall Model

The sand is placed in the test tank by dry pluviation for achieving the desired density uniformly. The sand is spread in the model box by raining through a hopper as shown in Figure 3.11. To determine the relative density of the backfill, density cans (54 mm in diameter, 34 mm in depth) are used as shown in Figure 3.12. These cans are placed in a staggered scheme in the vertical direction to avoid boundary effects. At the end of each experiment, these cans are carefully taken out and weighed. Then, the relative density is calculated (ASTM D-2049).



Figure 3.11. Placement of the Sand by Pluviation Method.



Figure 3.12. Placement of Density Cans on the Backfill.

Desired relative density of the backfill can be obtained by adjusting the falling height of the sand during pluviation. However, only minor densification can be achieved by increasing the pluviation height. Therefore, for models that require denser backfills, backfill soil was compacted using an electrical hand compactor as shown in Figure 3.13. The degree of density in the backfill can be adjusted by adjusting compaction time.



Figure 3.13. The Compaction Method.

3.6. Conducting the Tests in the Small Scale Retaining Wall Model

After the preparation of the backfill, recording and lightning devices are prepared for capturing images from the test. Then the model test starts by initiating the translation of the model wall either away from the backfill or towards the backfill. The movement direction of the wall depends on the desired failure type, active or passive. As the wall moves, images of the backfill at constant intervals are capture for image analysis (Figure 3.14). The camera can capture two high-quality (24 megapixels) images per second in continuous mode. This rate is more than sufficient for identification of shear bands and failure surfaces through image analysis.



Figure 3.14. The Image Capture During the Test.

4. VISUALIZATION OF FAILURE IN ACTIVE STATE

Considering the image processing tools used in geotechnical studies, the principal point that governs the accuracy and precision of the results is the ability of the algorithm to track the particles during the test. GeoPIV is a MatLab module that is used for measuring deformations in geotechnical bodies by implementing Particle Image Velocimetry (PIV) technique and tracking the texture of the soil (i.e. the spatial variation of brightness). Details of GeoOIV is given in White *et al.*, (2003).

For the analysis of deformations using GeoPIV, the first image is divided into a mesh of small patches that have their unique color signature at time t1, as shown in Figure 4.1. Displaced locations of the all patches in the subsequent image are determined through defining a larger patch (i.e. neighboring zone of the patch at time t_2) and correlating this area with subjected initial patch. The location that has the maximum correlation is considered as the displaced position of the patch. The difference between the target patch coordinates, measured in pixels, and the reference patch is calculated and visualized by the displacement vector as shown in Figure 4.1. The location of the correlation peak is established to sub-pixel precision by fitting a bicubic interpolation around the highest integer peak. This operation is repeated for the entire mesh of patches within the image, then repeated for each image within the series, to produce complete trajectories of each test patch.

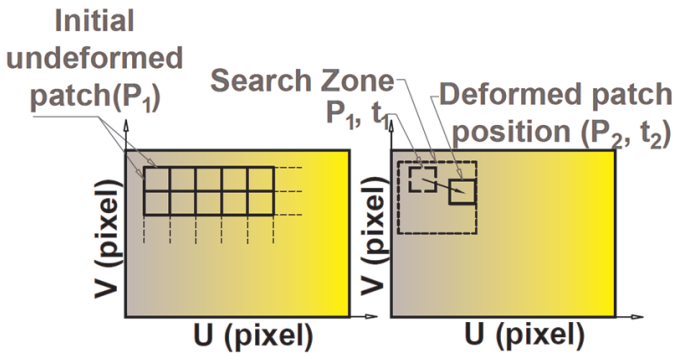


Figure 4.1. Determination of Displacement Vector Field (i) Pixel Intensity Variation Signature (ii) Displacement Vector.

GeoPIV provides information on relative deformations of the particles by means of strain maps. It measures strain distribution through high-resolution photogrammetry. GeoPIV creates a triangular mesh of elements which link the center of patches with its neighbouring patches (Jackson 2010). Relative patch displacement causes extension or compression of these elements; this is used to calculate various components of strain that include the maximum shear strain, shear strain, linear strain, or volumetric strain. Figure 4.2 shows the triangular element mesh (in uv-space) after "wild" vectors and associated patches within the window were removed during the cleaning process.

Equation 4.1 presents the maximum shear strain calculated from the relative extension and compression of elements linking adjacent patches.

$$\gamma = \sqrt{(\varepsilon_y - \varepsilon_x)^2 + \gamma_{xy}^2} \tag{4.1}$$

where γ is maximum shear strain, ε_2 and ε_y are linear strains in the x and y directions respectively, and γ_{xy} is the shear strain in the x-y plane.

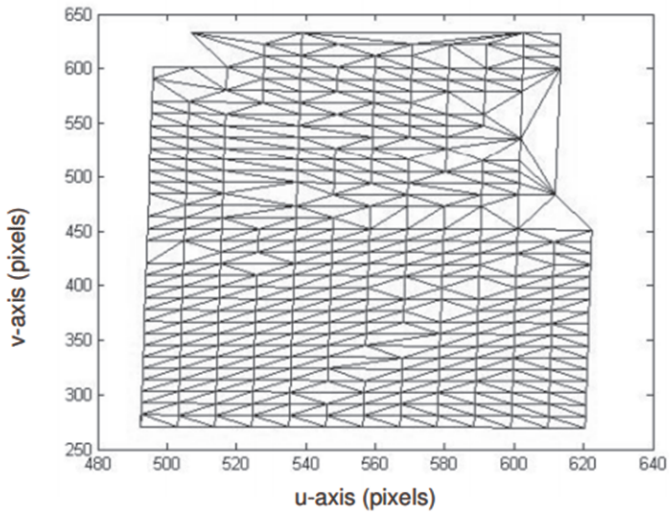


Figure 4.2. Triangular Element Mesh for Strain Calculation Plotted in X_y Coordinates. Note That Because Some "Wild" Vectors Were Evident in the Displacement Plots, the Associated Patches Have Been Removed From the Element Mesh (Jackson 2010).

Patch size is an important factor for the precision of PIV results, since it is a strong function of defined patch size in initial mesh; the larger the patch size, the greater the precision. A sequence of images for one specific test was analysed considering four patch sizes to determine the most appropriate patch size for subsequent analysis. The patches measured in pixels sized 16 by 16, 32 by 32, 64 by 64 and 128 by 128 pixels. The calibrated shear strain and vector plots for each analysis and also illuminated sand particles are shown in Figure 4.3. At small patch sizes, unnecessary details are visible in strain maps that are the result of generated wild vectors in displacement field. Moreover, another disadvantage of very fine mesh is the long-time consumed during the analysing process. However, with larger patch sizes, there are missing details in displacement field and also a crude shear strain map is observed (i.e. 128x128 pixel patches). A decision is made on choosing 64x64 pixel sized patches, of which optimized and appropriate for failure surface determination. Chosen patch size provides a sufficient texture for detecting deformations in granular backfill.

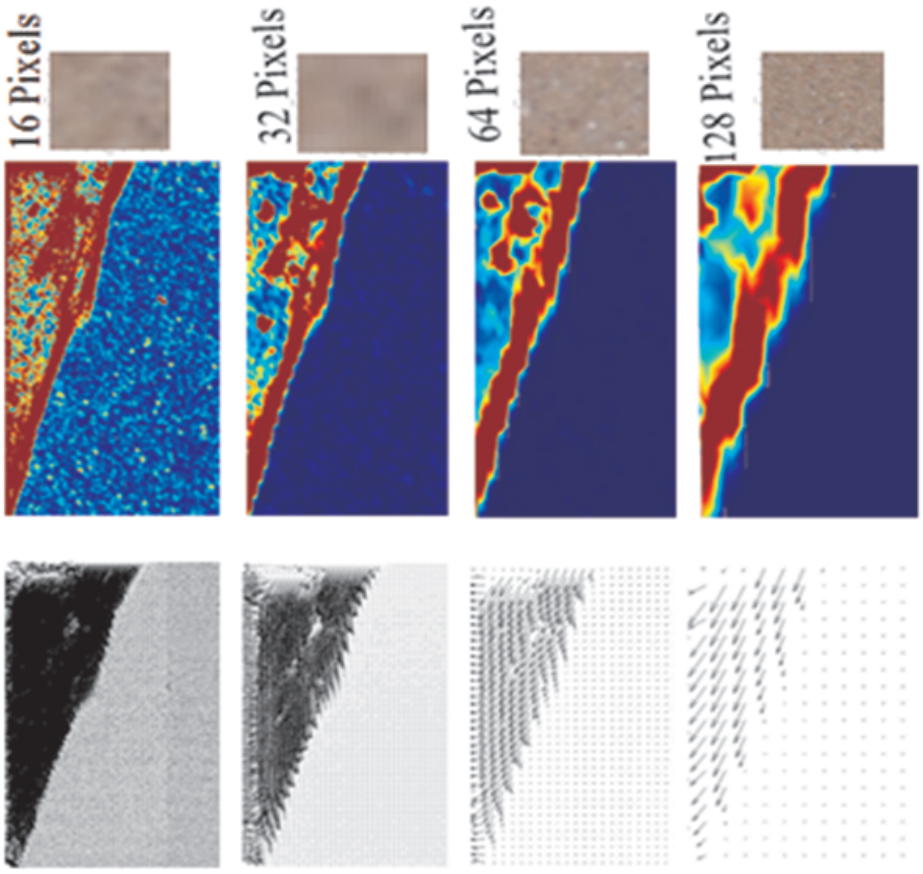


Figure 4.3. Patch Size Effect on Geopiv Results.

GeoPIV provides both shear and volumetric strain distribution maps. Shear strain maps are useful for observing strain localization and identifying the formation of shearing zone. On the other hand, volumetric strain maps give idea on whether the deformations are contractive or dilative. As displayed in Figure 4.4, it is clear that with wall movement a shearing wedge appears, along which the maximum shearing deformations concentrate.

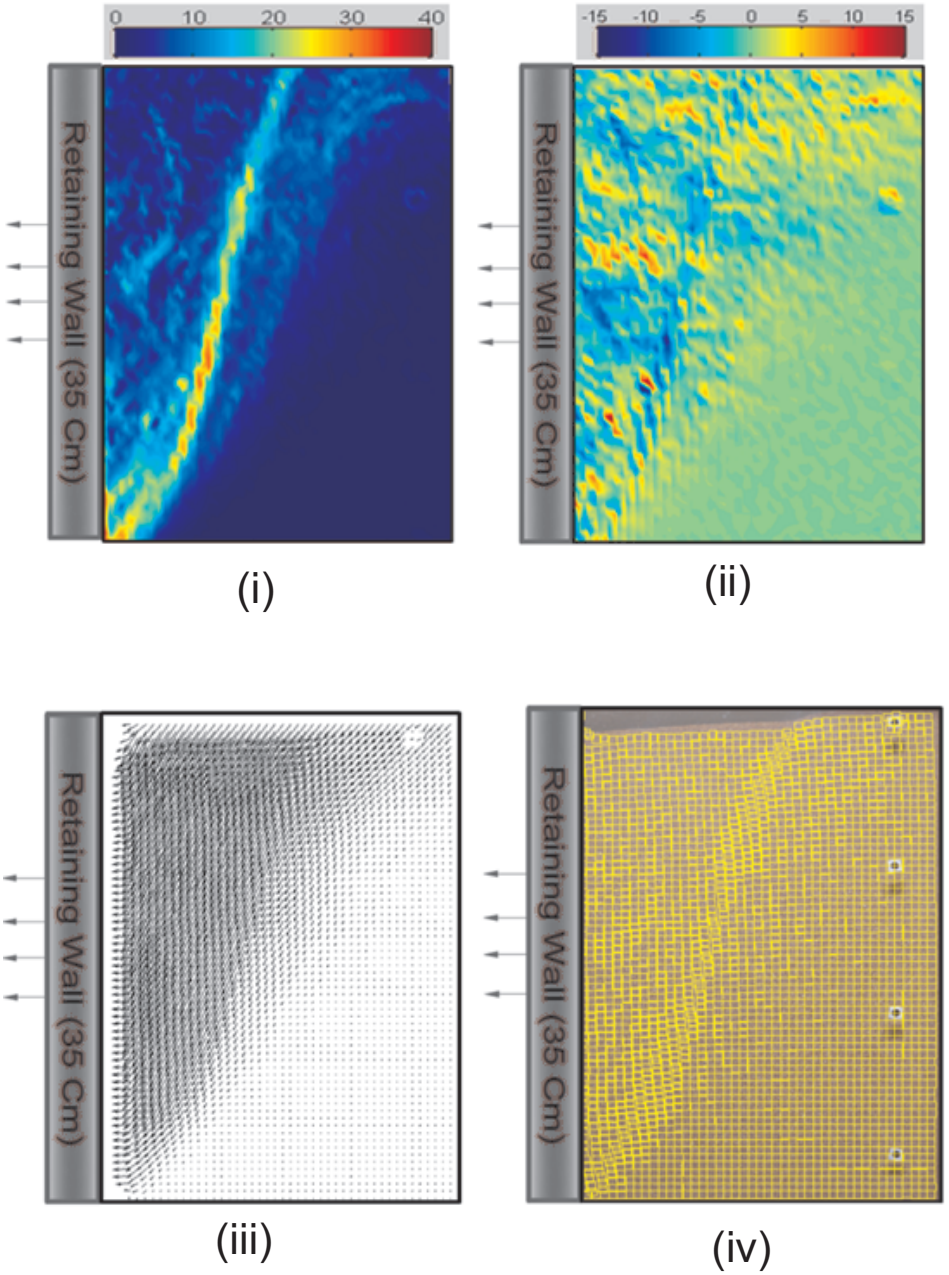


Figure 4.4. Typical PIV Results for Active Retaining Wall Translation (i) Shear Strain (ii) Volumeti Strain (iii) Vector Field (iv) Deformed Patches Profile.

Using the shear and volumetric strain maps, failure surface can be identified by following the locus of maximum strain points. Evaluating defined failure surfaces, it is observed that greater backfill densities correspond to steeper and more intense shear bands during active wall failures (Figure 4.5). This is an outcome of higher internal friction (ϕ'_p) and dilatancy (ψ_p) angles associated with greater relative densities. This fact is also supported by Loukidis and Salgado (2012) in their study based on finite element model simulations. Analyzing the consecutive stages of the test from start to finish for tests with high dilatancy angles, it has been observed that deformations concentrate to a narrow continuous region even during the initial stages of the test. This region, during the stages leading up to failure, evolves into failure surface. As soon as a failure surface forms, deformations become restricted to the region between the failure surface and the wall as shown in Figure 4.6. This area is referred to as the failure wedge.

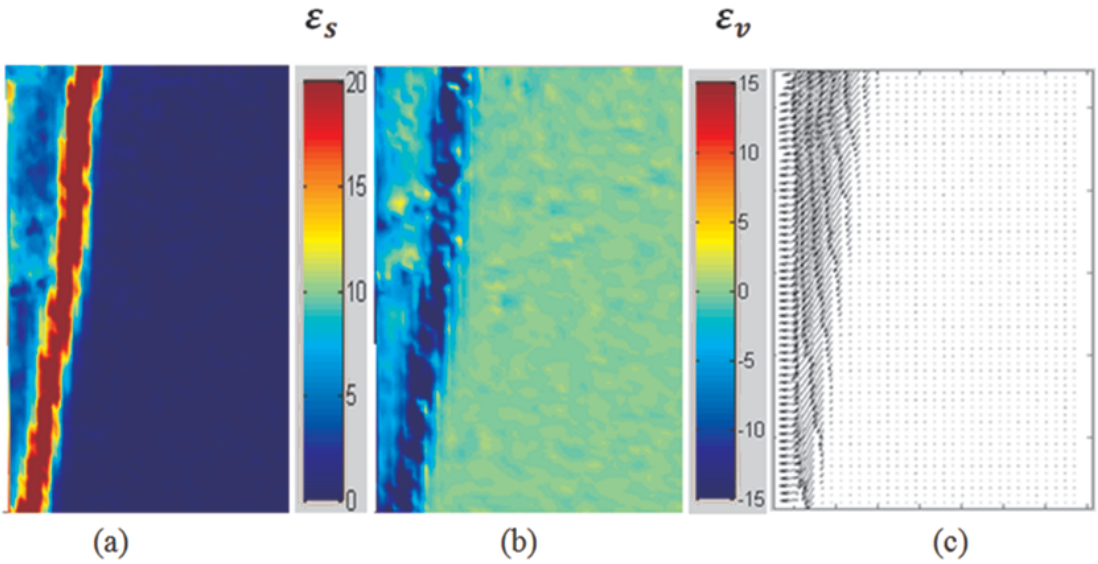


Figure 4.5. Localization of Cumulative Strains In Initially Dense Sand Based on as Obtained From PIV Analyses (a) Distribution of Shear Strains (ε_s), b) Distribution of Volumetric Strains (ε_v), (b) Vector Field of Deformation.

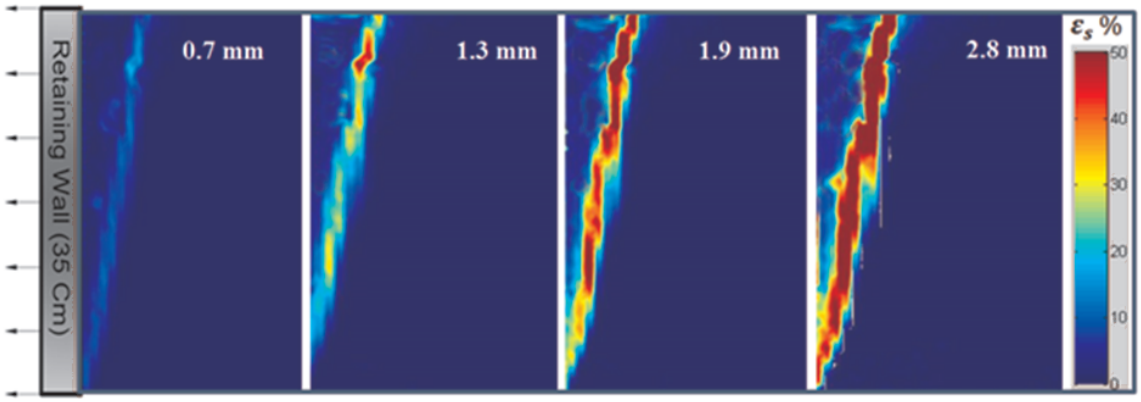


Figure 4.6. Shear Strain Concentration and Failure Surface Evolution with Respect to Rigid Retaining Wall Movement.

As observed in Figure 4.5 and Figure 4.7, both dilative and contractive deformations can be identified on volumetric strain maps obtained from PIV analyses. Accordingly along the failure band, volumetric deformation is dominantly dilative for dense backfills (Figure 4.5b) and dominantly contractive for loose backfills (Figure 4.7b). Evidently in Figure 4.7b, failure surface is hardly distinguishable for loose backfills unlike for dense backfills in which failure surfaces are clearly visible. This shows the influence of dilatancy on localization of shear strains in granular materials. Based on this observation, it is possible to propose that the geometry of shear planes can be quantified as functions of dilatancy angle. This proposition has its roots in plasticity theory for geomaterials (Atkinson 1981). A recent study by Niedostatkiewicz *et al.*, (2011) also supports the idea that deformation in shear zones is always related to dilatancy.

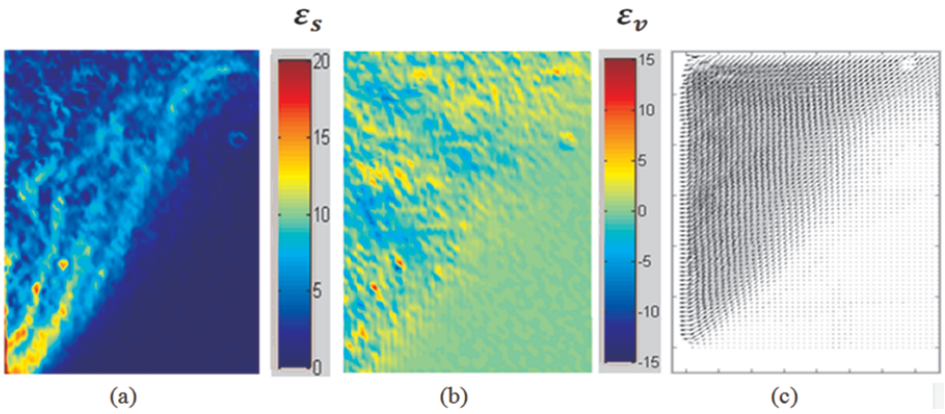


Figure 4.7. Localization of cumulative strains in initially loose sand as obtained from PIV analyses (a) shear strain (ε_s), (b) volumetric strains (ε_v), (c) vector field of deformation.

From the analyses of the shear and volumetric strain maps, shearing zone formed during failure of the backfill can be detected via GeoPIV analyses. In other word, it is possible to observe the evolution of failure surface geometry with wall displacement.

4.1. Quantification of Failure Surface Geometry

Identified failure surfaces can be quantified by transferring them to a normalized coordinate system as shown in Figure 4.8. In accordance with this purpose, the origin of the coordinate system is placed at the bottom of the model wall. By normalizing the coordinate system with respect to the height of the wall (H_w), all dimensions are made dimensionless. Outer edge of failure surfaces are marked with colored dots and quantified for both X and Y directions as shown in Figure 4.8a. As a result of quantification of failure surfaces, coordinates of the points along the failure surfaces are identified in terms of both B (away from the model wall) and H (parallel to the plane of the model wall) as shown in Figure 4.8b. All measurements are made with respect to the position of the wall prior to any displacement.

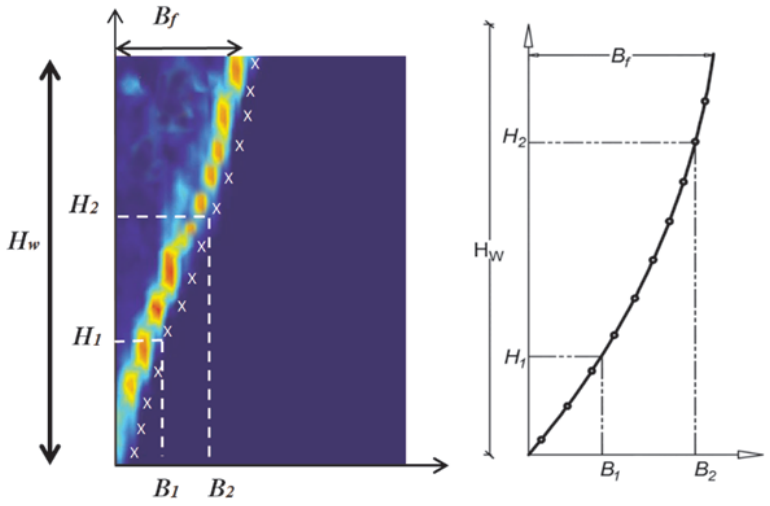


Figure 4.8. Detection of the Failure Surface Geometry a) As Plotted on the Shear Strain Map b) As Shown with an Illustration.

4.2. Determination of the Failure Surface Geometry Based on Dilatancy Angle

In this study, fitting curves were used for mathematically defining the geometries of failure surfaces. These curves are in good agreement with the geometries of failure surfaces determined using PIV method. Conventionally, shapes of active failure surfaces are assumed to be linear. However, reality deviates from this assumption as evidenced by the results of the model tests. In addition to this study, previous researchers also noted that active failure surfaces formed in backfills have parabolic shapes. As a result, Spangler and Handy (1984) proposed a 2^{nd} order parabolic function for the determination of failure surface shapes. The form of the 2^{nd} order parabolic function is shown in Equation 4.2.

$$z = aB^2 + bB + c \tag{4.2}$$

where z defines the vertical coordinate and B defines the horizontal distance from the retaining wall to the failure surface. Using the boundary conditions, constants of the

parabolic failure function can be obtained as follows:

$$z = H_w \rightarrow B = 0 \tag{4.3}$$

$$z = H_w \rightarrow \frac{dz}{dB} = -\tan\alpha \tag{4.4}$$

$$z = 0 \rightarrow B = (a_b)H_w \cot\alpha \tag{4.5}$$

where a_b is defined as the ratio of B_f to x which is illustrated in Figure 4.9. Using the above three boundary conditions, the constants a, b, and c are obtained as follows:

$$a = \left[(a_b - 1)/(a_b^2 H_w)\right] \tan^2\alpha \tag{4.6}$$

$$b = -\tan\alpha \tag{4.7}$$

$$c = H_w \tag{4.8}$$

Inserting the constants given in Equation 4.6, Equation 4.7 and Equation 4.8 into Equation 4.2 gives Equation 4.9.

$$z = \left(\left[\frac{(a_b - 1)}{(a_b^2 H_w)}\right] \tan^2(\alpha)\right) B^2 - \tan(\alpha)B + H_w \tag{4.9}$$

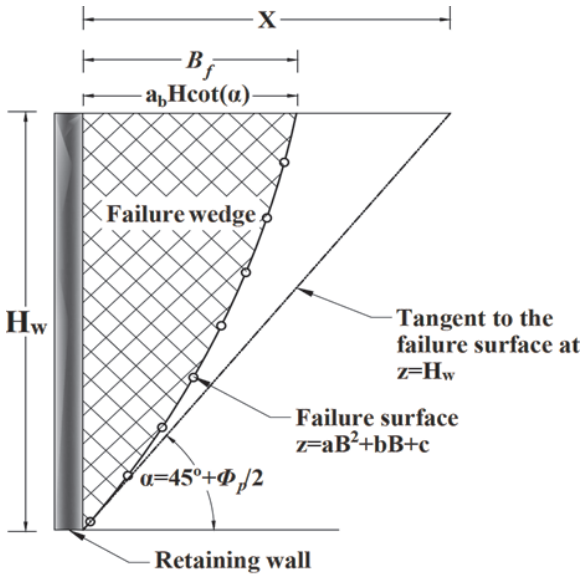


Figure 4.9. Shape of the Assumed 2nd Order Parabolic Failure Surface (Altunbaş 2014).

In consideration of proposition of Spangler and Handy (1984), Altunbaş (2014) proposed a parabolic function based on dilatancy angle. According to Altunbaş (2014), the active failure surface geometry is dependent on the dilatancy angle. To find out a relationship between dilatancy angle (ψ) and the ratio of B_f to x (a_b) in the parabolic function, a_b values obtained for each test. The relationship between dilatancy angle (ψ) and the ratio of B_f to x (a_b) is shown in Figure 4.10.

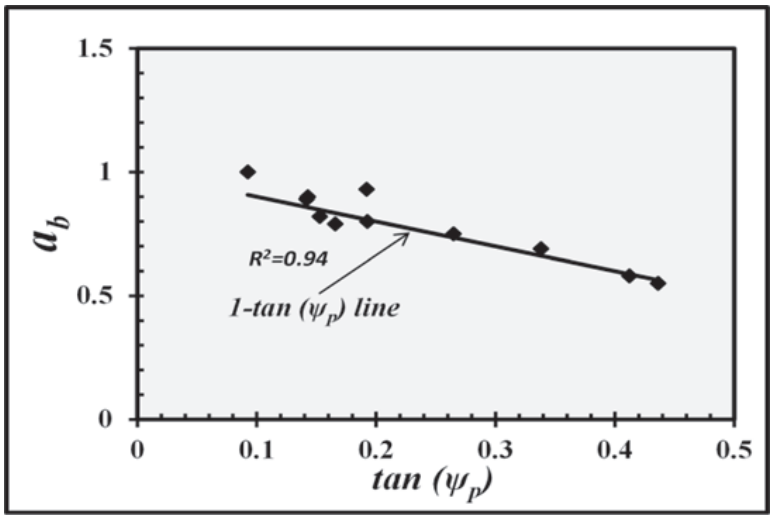


Figure 4.10. a_b-tan(ψ_p) Relationship Obtained Using the Data Gathered From Retaining Wall Model Study (Altunbaş 2014).

As it is seen in Figure 4.10, the empirical data agrees with the relationship shown as Equation 4.10.

$$a_b = (1 - \tan\psi_p) \tag{4.10}$$

By using the ratio of B_f to x (a_b) based on the dilatancy angle (ψ) in Equation 4.9, the function that provides the calculation of active failure surface geometry in terms of ϕ'_p, H_w and .Hw is shown in Equation 4.11.

$$z = \left(\left[\frac{(-\tan(\psi_p))}{((1 - \tan(\psi_p))^2 H_w)} \right] \tan^2(45 + \frac{\phi'_p}{2}) \right) B^2 - \tan(45 + \frac{\phi'_p}{2}) B + H_w \tag{4.11}$$

Equation 4.11 proposed by Altunbaş (2014) was derived as a result of many tests conducted on the backfills at different relative densities. However, all the tests were conducted using the same wall. Thus, the wall friction was the same at all the tests. For this reason, it was controlled if the wall friction had an effect on Equation 4.11 that gives the failure surfaces geometry dependent on dilatancy angle or not. To control it, the wall was covered with a sand paper whose friction angle with the backfill is about 35^o. Then the same tests were conducted again. The results for the tests with the wall friction angle of 21^o and 35^o are compared. The results for the comparisons are shown in Figure 4.11. As a result of the comparisons, it can be said that a change in wall friction does not affect the failure surface geometry. It means that Equation 4.11 proposed by Altunbaş (2014) is valid for all the wall friction angles.

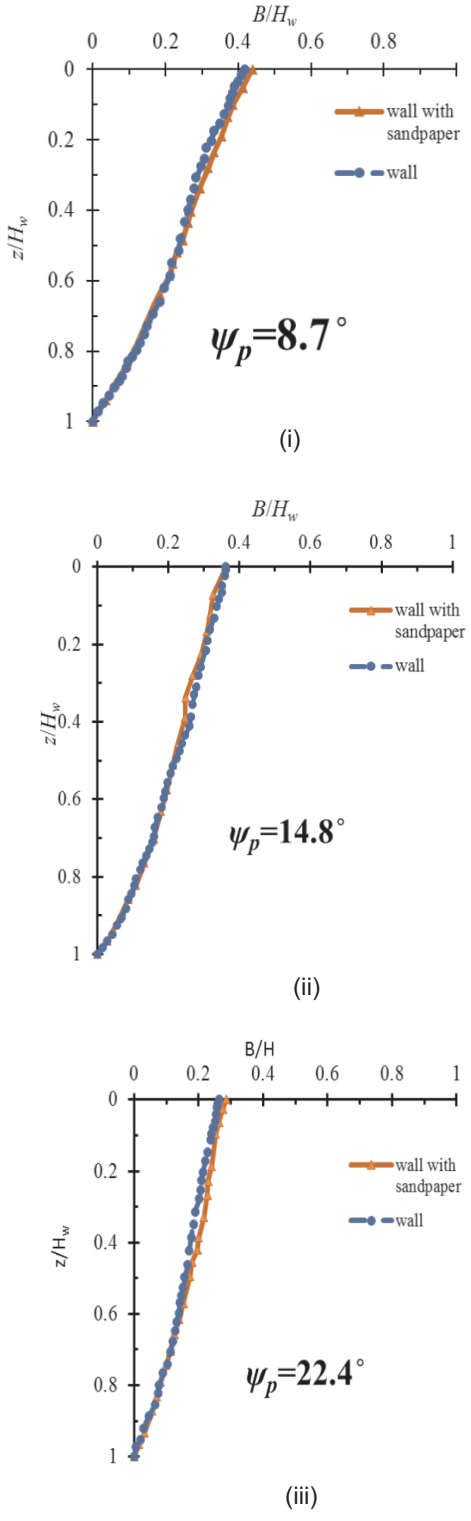


Figure 4.11. The Comparison of the Tests in Which the Wall and the Wall With Sand Paper for (i) Loose Bacfill (ii) Medium Dense Backfill and (iii) Dense Backfill.

5. A NEW METHOD TO CALCULATE THE ACTIVE FORCES ACTING ON THE WALL

Active lateral earth forces are calculated by using the equilibrium of the forces acting on the soil mass within the failure wedge. The forces acting on the soil mass consist of the force exerted by the wall, interface friction between the backfill and the plexiglass, normal and shear forces between the failing wedge and surrounding soil. Figure 5.1 shows the force equilibrium.

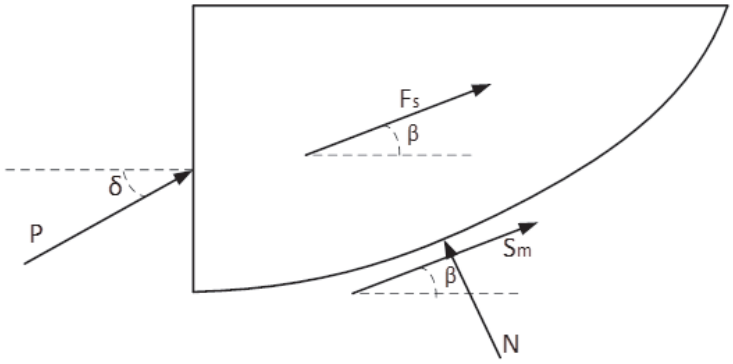


Figure 5.1. Forces Acting on Soil Mass in Active Failure State.

where is the W weight of the soil mass on the failure surface, is the δ the friction angle between the backfill and the wall, is the N the normal force on the base of the slice, is the S_m = the shear force on the base of the slice, is the F_S the friction force between the backfill and the side surface of the tank whose material is plexiglass, is the β the slope angle of the base of the slice.

For correct determination of the forces acting on the wall, the method of slices was used. The forces acting on the wall are calculated according to the failure surfaces identified depending on dilatancy angle (ψ_p) of the backfill. Soil mass above the identified failure surface was divided into 5 mm wide slices. For the calculation of active forces acting on the wall,

$$P \times cos\delta = \Sigma\,(N \times sin\beta) - \Sigma\,(S_m \times cos\beta) - \Sigma\,(F_S \times cos\beta) \tag{5.1}$$

One of the parameters necessary for calculation of the force acting on the wall is the sum of the normal force on the base of the each slice. (Rahardjo 1984). To calculate the normal force acting on the base of the slice, equilibrium of horizontal and vertical components of all the forces acting on the slice is utilized. The forces acting on the slice were shown in Figure 5.2 by considering the friction force between the plexiglass side of the tank and the slice.

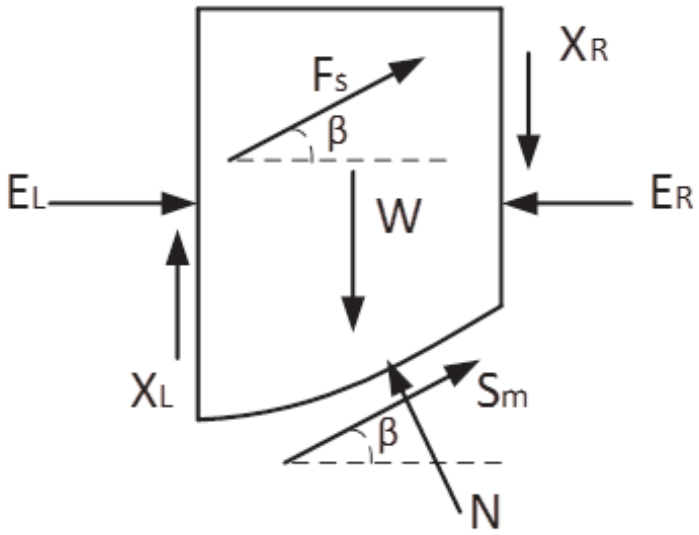


Figure 5.2. The Forces Acting on a Slice on the Failure Surface in Active Case.

where is the W weight of the slice, is the N the normal force on the base of the slice, is the S_m = the shear force on the base of the slice, is the F_s the friction angle between the backfill and the plexiglass surface, is the E_L the horizontal normal interslice forces on the left side, is the E_R the horizontal normal interslice forces on the right side, is the X_L the vertical shear interslice forces on the left side, is the X_R the vertical shear interslice forces on the right side, is the β the angle between the tangent to the center of the base of the slice and the horizontal.

5.1. Identifying the Slope Angle of the Base of the Slice

To calculate the normal force on the base of the slice, the magnitudes and directions of all the forces acting on the slice have to be described. For this aim, the slope of the base of the slice (β) is determined. To determine the slope of the base of the

slice, the geometry of the failure surface which the slice is above is used. The geometry of the failure surface is identified depending on peak dilatancy angle (ψ_p) by using the Equation 5.2 proposed by Altunbaş *et al.*, (2014).

$$Z = \left(-\tan\psi_p \Big/ \left((1-\tan\psi_p)^2 \times H_w\right)\right) \times (\tan\alpha)^2 \times B^2 - \tan\alpha \times B + H_w \qquad (5.2)$$

where is the H_w the height of the wall, is the α 45+$\phi'_p/2$, is the ψ_p peak dilatancy angle.

The coordinate values are used to calculate the slope of the center of the base of the n^{th} slice as shown in Figure 5.3. Then slope of the base of the n^{th} slice (tan β) can be calculated using Equation 5.3.

$$tan\beta = \frac{y_n - y_{n+1}}{x_{n+1} - x_n} \qquad (5.3)$$

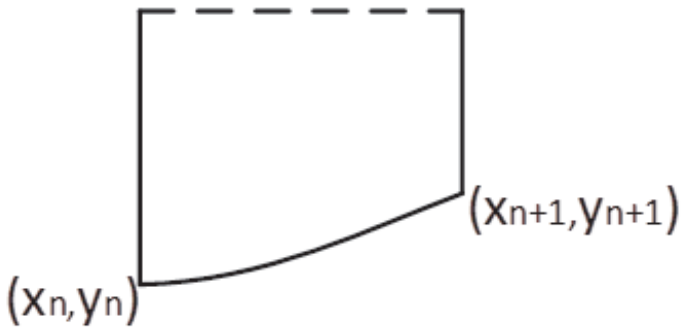


Figure 5.3. The Coordinates of the Base Corners of n^{th} Slice.

The relationship between the coordinates of the base corners of the n^{th} slice can be described using Equation 5.2 proposed by Altunbaş *et al.*, (2014). This relationship is shown in Equation 5.4.

$$y_n = \left(-\tan\psi_p \Big/ \left((1-\tan\psi_p)^2 \times H_w\right)\right) \times (\tan\alpha)^2 \times {x_n}^2 - \tan\alpha \times x_n + H_w \qquad (5.4)$$

Substituting the relationship between x and y coordinates of the slice base corners into Equation 5.4 and solving for the slope (tanβ) yields

$$tan\beta = \frac{\left(-\tan\psi_p / \left((1-\tan\psi_p)^2 \times H_w\right)\right) \times (\tan\alpha)^2 \times (x_n - x_{n+1})^2}{x_{n+1}-x_n} \Bigg/ \frac{-\tan\alpha \times (x_n - x_{n+1}) + H_w}{x_{n+1}-x_n} \tag{5.5}$$

Slope angle β can also be calculated using Equation 5.6.

$$\beta = \tan^{-1} \left[\frac{\left(-\tan\psi_p / \left((1-\tan\psi_p)^2 \times H_w\right)\right) \times (\tan\alpha)^2}{x_{n+1}-x_n} \right] \Bigg/ \left[\frac{\times \left(x_n - x_{n+1}\right)^2 - \tan\alpha \times (x_n - x_{n+1}) + H_w}{x_{n+1}-x_n} \right] \tag{5.6}$$

5.2. Identifying The Shear Force on the base of the Slice and the Friction Force between the Backfill and the Plexiglass Surface

The shear force on the base of each slice can be computed in accordance with Mohr-Cloumb failure criterion:

$$S_m = \frac{S \times (c' + \sigma_n \times tan\phi')}{FS} \tag{5.7}$$

where is the S base length of the slice, is the FS: Factor of Safety

Since this study considers clean sands c'=0 and there is no design factor of safety, therefore FS=1; by using the equation of $T = sx\sigma_n$, the shear force at the base of the slice (S_m) can be identified in terms of normal force at the base of the slice (N):

$$S_m = N \times tan\phi' \tag{5.8}$$

The friction force between the slice and the plexiglass surface can be determined

using Equation 5.9.

$$F_S = \frac{1}{4} \times \gamma \times (y_n^2 + y_{n+1}^2) \times b \times K_0 \tag{5.9}$$

where is the γ Unit weight of backfill, is the y_n Length of the left side of the n^{th} slice, is the y_{n+1} Length of the right side of the nth slice, is the K_o lateral earth pressure coefficient at rest, is the b the width of the n^{th} slice.

Therefore, the force on the wall can be calculated via Equation 5.10:

$$P \times cos\delta = (N \times (sin\beta - tan\phi' \times cos\beta) - F_s \times \cos\beta) \tag{5.10}$$

where is the W Weight of the wall, is the K_o Lateral earth pressure coefficient at rest.

5.3. Identifying the Weight of a Slice

The weight of a slice (W) is required for calculating the normal force at the base of a slice. To do determine the weight of the slice, the area of the slice (A) must be calculated first. Using the coordinate values of the base corners of the n^{th} slice shown in Figure 5.3 and solving for the area of the n^{th} slice gives

$$A = \frac{(y_n + y_{n+1}) \times (x_{n+1} - x_n)}{2} \tag{5.11}$$

By substituting the relationship between x and y coordinates of the base corners of the n^{th} slice into Equation 5.11, the formula shown Equation 5.12 is obtained to calculate the area of the n^{th} slice depending on the failure surface geometry.

$$A = \frac{\frac{(-\tan\psi_p / \left((1-\tan\psi_p)^2 * H_w\right) \times (\tan\alpha)^2 \times (x_n - x_{n+1})^2}{2}}{\frac{-\tan\alpha \times (x_n - x_{n+1}) + H_w) \times (x_{n+1} - x_n)}{2}} \tag{5.12}$$

The weight of the slice (W) is computed by multiplying the computed area of the

slice (A) with the unit weight of the backfill (γ):

$$W = A \times \gamma \tag{5.13}$$

5.4. Interslice Force Function for the Active Earth Force

Interslice shear forces are obtained using an assumption regarding the relationship between interslice shear forces and normal interslice forces. This relationship can be described as follows using an arbitrary interslice force function ($f(x)$):

$$\frac{X}{E} = \lambda f(x) \tag{5.14}$$

where is the $f(x)$ a mathematical function that describes the relationship between the shear force X and normal force E on the slides of each vertical slice of the sliding mass, is the x length from the starting point of the failure surface to a desired point on the failure surface (Figure 5.4), λ a coefficient representing the fraction of the function used in the calculation of the lateral earth force.

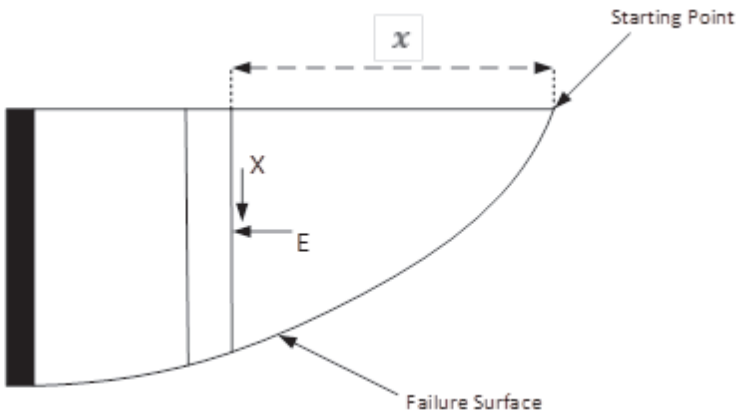


Figure 5.4. The Length from the Starting Point of the Failure Surface to a Desired Point on the Failure Surface.

The magnitude of the force function stars with zero at the starting point of the

failure surface (the point where the failure surface emerges at the ground surface). However, the magnitude of the force function increases up to the tangent of the wall-backfill interface friction angle (tan δ) at the wall. Between these two boundaries, the interslice force function is assumed to change linearly. The displacement of the soil mass results in positive shear stresses. This behavior causes the positive interslice force ratios for the entire sliding mass in the active case. Using Equation 5.14 to define the interslice force ratio, the λ variable can be set equal to the tangent of the wall friction angle (tan δ) and the interslice force function, $f(x)$, will reach a maximum value of 1.0 at the wall. To evaluate the effect of the interslice force function, the λ variable was varied from 0 to tan (δ). When using λ equal to tan (δ), the relationship for the interslice force function can be expressed as follows:

$$\frac{X}{E} = (tan\delta) \times \frac{x}{B_f} \tag{5.15}$$

where is the B_f horizontal length along the failure surface (Figure 5.5).

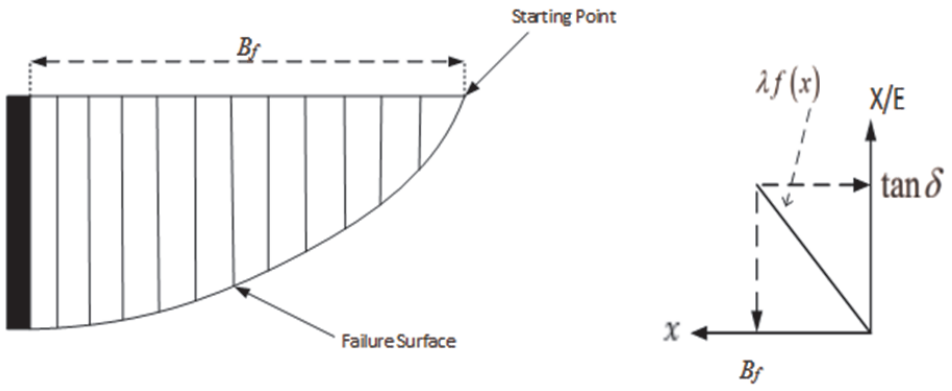


Figure 5.5. The Interslice Function for Active Case.

The horizontal length along the failure surface also depends on the failure surface geometry. Thus, the length can be identified in terms of the dilatancy angle as shown in Equation 5.16.

$$B_f = (-\tan\psi_p) \times H_w \times cot\alpha \tag{5.16}$$

5.5. Identifying the Normal Force Acting at the Base of the Slice

The summation of forces in the vertical direction for each slice gives

$$W + X_R - X_L - S_m \times sin\beta - N \times cos\beta - F_S \times sin\beta = 0 \tag{5.17}$$

Substituting Equation 5.8 into Equation 2.17 gives

$$W + X_R - X_L - N \times tan\phi' \times sin\beta - N \times cos\beta - F_s \times sin\beta = 0 \tag{5.18}$$

Solving (X_L-X_R), the difference between the shear interslice force on the left and right sides of the slice gives

$$X_R - X_L = N \times (cos\beta + tan\phi' \times sin\beta) + F_s - W \tag{5.19}$$

However, the horizontal equilibrium of forces on each slice is used to compute the interslice normal forces. The summation of forces in the horizontal direction for each slice gives

$$E_R - E_L - S_m \times cos\beta + N \times sin\beta - F_S \times cos\beta = 0 \tag{5.20}$$

Substituting Equation 5.8 into Equation 5.20 gives

$$E_R - E_L - N \times tan\phi' \times cos\beta - F_s \times cos\beta + N \times sin\beta = 0 \tag{5.21}$$

To determine the difference between the interslice normal forces on the left and right sides of the slice, Equation 5.21 is turned into

$$E_R - E_L = N \times (tan\phi' \times cos\beta - sin\beta) + F_s \times cos\beta \tag{5.22}$$

The relationship between (X_R-X_L) and (E_R-E_L) ,obtained by using respectively Equation 5.19 and Equation 5.22, is determined by using an assumption that the lengths from the starting point of the failure surface to right and left sides of the slice (x) are same. The assumed length is equal to the horizontal distance between the starting point of the failure surface and the midpoint of the slice. This length is calculated using the arithmetic mean of the described lengths for right and left sides of the slice Figure 5.6:

$$x = \frac{x_R + x_L}{2} \tag{5.23}$$

where is the x_R The length from the starting point of the failure surface to right side of the slice, is the x_L The length from the starting point of the failure surface to left side of the slice, is the x The length from the starting point of the failure surface to midpoint of the slice.

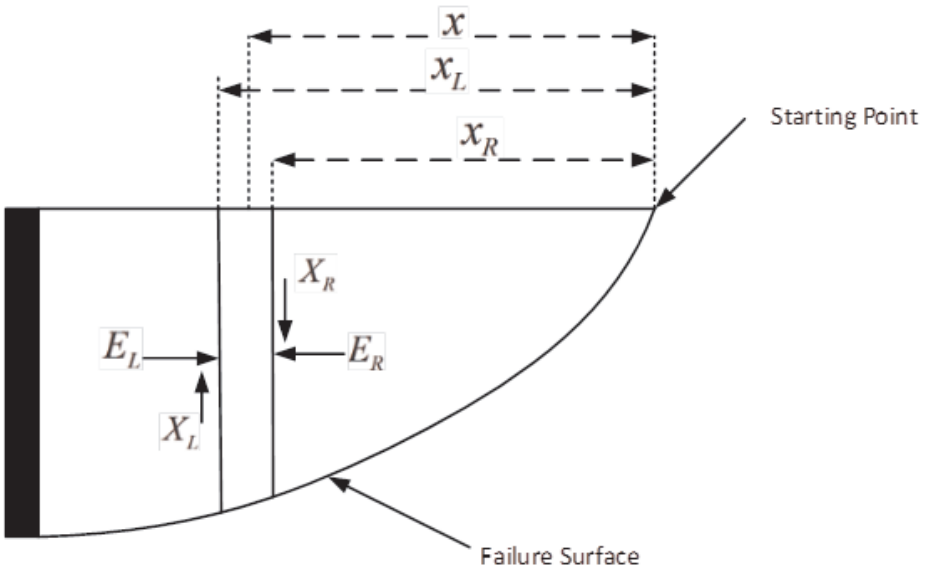


Figure 5.6. The Assumed Common Length for Right and Left Sides of the Slice.

By using the assumption together with Equation 5.15, the relationship between (X_R-X_L) and (E_R-E_L) is described as follows:

$$\frac{X_R - X_L}{E_R - E_L} = (tan\delta) \times \frac{x}{B_f} \tag{5.24}$$

Substituting Equation 5.22 into Equation 5.24 gives

$$X_R - X_L = (N \times (tan\phi' \times cos\beta - sin\beta) + F_s \times cos\beta) \times (tan\delta) \times \frac{x}{B_f} \tag{5.25}$$

Combining Equation 5.19 and Equation 5.25 enables to obtain a new equation that provide to determine normal force acting on the base of the slice:

$$\begin{aligned} &N \times (cos\beta + tan\phi' \times sin\beta) + F_s \times \sin\beta - W \\ &= (N \times (tan\phi' \times cos\beta - sin\beta) + F_s \times cos\beta) \times (tan\delta) \times \tfrac{x}{B_f} \end{aligned} \tag{5.26}$$

Equation 5.27 obtained by deriving from Equation 5.26 gives the normal force acting on base of each slice.

$$N = \frac{\left(F_s \times \left(\frac{\cos\beta \times \tan\delta \times x}{B_f} - \sin\beta\right) + W\right)}{\left(cos\beta + tan\phi' \times sin\beta + \frac{\tan\delta \times x \times (\sin\beta - tan\phi' \times \cos\beta)}{B_f}\right)} \tag{5.27}$$

Length of the failure surface (B_f) and slope angle of base of each slice (β) in Equation 5.27 is computed by using Equation 5.16 and Equation 5.6, respectively. According to these equations, length of the failure surface (B_f) and slope angle of base of each slice (β) depend on dilatancy angle. Thus, normal force acting on the base of each slice also depends on dilatancy angle of the backfill. By using Equation 5.27 derived to compute the normal force acting on the base of each slice that depens on dilatancy angle the total lateral force acting on the wall can be calculated by using Equation 5.28.

$$P \times cos\delta = \Sigma\,(N \times (sin\beta - tan\phi' \times cos\beta) - F_s \times \cos\beta) \tag{5.28}$$

6. THE RESULTS FOR ACTIVE LATERAL EARTH THRUSTS

For evaluating the method, 10 small scale retaining wall model tests in active state were conducted. The common parameters for all the tests are shown in Table 6.1. However, some properties of the backfill vary from test to test. They were determined for each test and classified according to number of tests. The parameters for the active tests are shown in Table 6.2. Unit weight values are measured using the density cans inserted into the backfill. On the other hand peak dilatancy angles (ψ_p) are calculated using Equation 2.1 and peak friction angles are calculated using Equation 2.2.

Table 6.1. The Common Parameters for all the Tests.

Wall Friction Angle (δ)	21°
Pleksglass Friction Angle (θ)	23°

Table 6.2. The Specific Parameters of the Backfills Prepared for Active Tests.

Test No	Unit Weight (kN/m3) (kN/m^3)	Internal Friction Angle (°)	Dilatancy Angle (°)
1	15.2	35.92	10.87
2	15.25	35.94	10.91
3	14.9	34.85	8.13
4	14.87	34.83	8.07
5	15.05	35.35	9.41
6	15.68	37.47	14.85
7	14.61	33.74	5.28
8	16.18	38.97	18.68
9	16.72	40.42	22.41
10	16.91	40.87	23.57

6.1. Calculated Active Thrust Magnitudes

The active lateral thrust on the wall for each test was calculated by utilizing the new method explained in Chapter 5. Within the proposed method; the calculations were made by regarding the dimensions of small scale retaining wall model and the plane strain concept. Dilatancy angles (ψ_p), internal friction angles (ϕ_p) and unit weights (γ) of the backfills on which the tests were conducted were used as parameters. While dilatancy angles (ψ_p) and internal friction angles (ϕ_p) were calculated using the equation proposed by Çinicioğlu and Abadkon (2014), the unitweights of the backfills (γ) are measured during the tests. The interface friction angles developed between the sand backfill and the surfaces of the wall and the plexiglass shown in Table 6.1 were also used to compute the lateral earth forces. As a result of the calculations, the active lateral earth thrusts were determined for all the backfills at different relative densities. The values of these forces are shown in Table 6.3.

6.2. Measured Active Thrust Magnitudes

Apart from the calculation by using the proposed method, active earth thrusts are measured during the tests. These data were taken through the transducers mounted on the retaining wall as explained in Section 3.1. Then, the data were processed to determine the earth thrust acting on the wall at the time of failure. The active lateral earth forces obtained through this way for all the tests are shown in Table 6.3.

6.3. Results for the Values of Active Lateral Earth Forces Acting on the Wall According to Rankine and Coloumb Theories

The theories suggested by Rankine (1857) and Coloumb (1776) are the most common methods to calculate the lateral earth pressures and forces. For this reason, the values of lateral earth forces for active and passive states were also calculated using Rankine (1857) and Coulomb (1776) methods. However, computations of the earth forces using these theories do not include the interface friction effect between the backfill and the plexiglass. On the other hand, this friction effect was considered while

the lateral earth forces were determined in this thesis.

In order to compare calculation and measurement results with the Rankine and Coloumb theories, the friction force between the backfill and the plexiglass should have been also added to the computation based on these theories. For this reason, the friction forces, that is calculated as indicated in Section 5.1.2., were subtracted from the active lateral earth forces computed according to theories of Rankine (1857) and Coloumb (1776). On the other hand, the friction forces between the backfill and the plexiglass surface were added to the passive lateral earth forces obtained using these theories. The active forces values obtained by considering the influence of side-wall friction are shown in Table 6.3.

Table 6.3. The Results for Active Lateral Earth Thrusts Obtained from the Calculation Method, the Measurement Method, and Rankine and Coloumb Theories.

Test	The Calculation Results	The Measurement Results	Rankine Results	Coloumb Results
No	(N)	(N)	(N)	(N)
1	202.6	191	235.4	198.4
2	202.5	186	235.3	198.3
3	209.2	196	240.8	202.2
4	209.4	198	241.1	202.4
5	205.8	194	238.6	200.7
6	192.2	182	227.9	193.1
7	215.6	200	246.7	206.4
8	180.6	156	221.1	188.2
9	167.8	154	214.7	183.6
10	163.4	143	212.9	182.3

7. CALCULATION OF PASSIVE FORCES ACTING ON THE WALL BY USING THE NEW METHOD

Determination of passive lateral earth forces acting on the wall plays a vital role on the design of the geotechnical structures. For this reason, many researchers had proposed to calculate passive lateral earth forces, e.g., Coloumb (1776), Rankine (1857), Caquot and Kerisel (1948), Janbu (1957), Terzaghi and Peck (1967), Shields and Tolunay (1973), Rahardjo and Fredlund (1984), Zakerzadeh (1999). In this study, passive lateral earth forces acting on the wall were computed by using the new method proposed in Chapter 5. Indeed, the method for calculation of passive lateral earth forces is almost the same as the method suggested for active cases in this thesis. However, the proposed calculation method needs modification in order to be used for passive problems.

7.1. Passive Failure Surface Geometries

The first step for calculating passive lateral earth thrust acting on the wall using the modified new method is the identification of passive failure surface geometries. It has been observed from the passive model tests that passive failure geometries can best be described using 2nd order parabolic functions (Figure 7.1). For this purpose, the same approach as in the case of Equation 4.2 for active cases is used for passive problems.

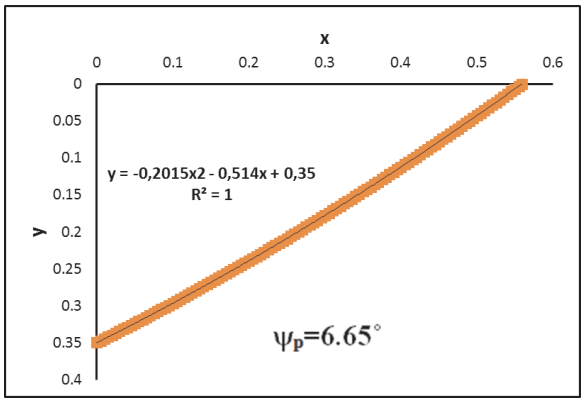


Figure 7.1. Passive Failure Surface Geometry Dependent on Dilatancy Angle.

However, the ratio of B_f to x (a_b) is different from active cases, as expected. For passive cases, Altunbaş (2014) suggested a relationship between peak dilatancy angle (ψ_p) and the ratio of B_f to x (a_b), using the a_b values obtained for each test. This relationship is shown as in Figure 7.2.

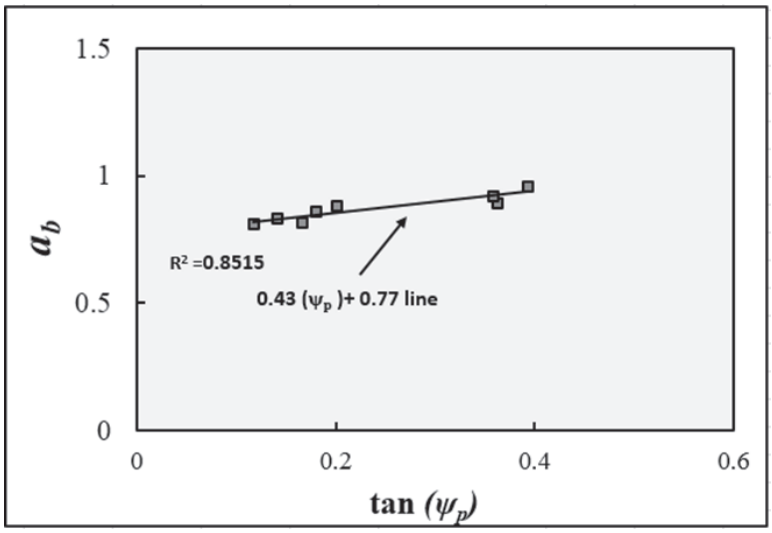


Figure 7.2. a_b-tan(ψ_p) Relationship Obtained Using the Data Gathered From Retaining Wall Model Study for Passive Cases (Altunbaş 2014).

As it is seen in Figure 7.2, the empirical data agrees with the relationship shown as Equation 7.1.

$$a_b = (0.43 \tan \psi_p + 0.77) \tag{7.1}$$

By using the ratio of B_f to x (a_b) based on the peak dilatancy angle (ψ_p) in Equation 7.1, the function that allows the calculation of passive failure surface geometry in terms of ϕ'_p, ψ_p and H_w is shown in Equation 7.2.

$$\begin{aligned} z = & \left(\left[\frac{0.23-(0.43\tan(\psi_p))}{((0.43\tan(\psi_p)+0.77)^2 H_w)} \right] \tan^2(45 - \tfrac{\phi'_p}{2}) \right) \\ & B^2 - \tan(45 - \tfrac{\phi'_p}{2}) B + H_w \end{aligned} \tag{7.2}$$

The effect of the wall friction on passive failure surface geometries has not investigated yet. It will be investigated in further studies. However, it is assumed that the constants

in Equation 7.1 are dependent on the wall-backfill interface friction angle.

7.2. Interslice Function at Passive State

For the passive case, the ratio of shear interslice force to interslice normal force (X E) at the point where the failure surface emerges at the ground level is zero, just as it is in active problems. However, this ratio at the end of the failure surface is equal to negative value of tangent of the friction between the backfill and the wall (-tanδ). The reason for this is that the shear force acting at the base of a slice (S_m) acts downward because the soil mass moves upward. Because of direction of such shear forces, the interslice force function is negative. As a result of the sign of the function, the relationship between shear and normal interslice forces is as shown in Equation 7.3.

$$\frac{X}{E} = -\left(tan\delta\right) \times \frac{x}{B_f} \tag{7.3}$$

7.3. Normal Force Acting at Base of a Slice

After identification of interslice function at the passive case, normal force acting at base of a slice is calculated using the identified interslice function. For computation of the normal force, the steps used for active case are followed. By adding Equation 7.2 and Equation 7.3 to the steps in the active case, Equation 5.25 was modified to enable a new equation for calculation of normal force acting at base of a slice. This new equation is shown in Equation 7.4.

$$N = \frac{\left(F_s \times \left(\sin\beta - \frac{\cos\beta \times \tan\delta \times x}{B_f}\right) + W\right)}{\left(cos\beta - tan\phi' \times sin\beta + \frac{\tan\delta \times x \times (\sin\beta + tan\phi' \times \cos\beta)}{B_f}\right)} \tag{7.4}$$

7.4. Passive Lateral Earth Thrust Acting on the Wall

It was shown in Chapter 5 that the horizontal components of the normal forces acting at base of all the slices on a soil mass give rise to lateral earth thrust on the wall in active case. This is also true for passive case. However, the horizontal components of the friction force between the backfill and the plexiglass and shear forces acting at base of all the slice also cause an increase in lateral earth thrust on the wall contrary to active case as illustrated in Equation 7.5.

$$P \times cos\delta = \Sigma\,(N \times sin\beta) + \Sigma\,(S_m \times cos\beta) + \Sigma\,(F_S \times cos\beta) \tag{7.5}$$

7.5. The Results For Passive Lateral Earth Thrusts

The proposed calculation method for passive cases was used to calculate passive lateral earth thrusts. The obtained results were controlled with the results for the small scale retaining wall model tests. Eight model tests were conducted within the aim of control. In the model tests, the common parameters, the wall friction and the plexiglass friction, are shown in Table 6.1. The parameters that vary from test to test are shown in Table 7.1. The specific parameters of the backfills prepared for passive tests.

Table 7.1. The Specific Parameters of the Backfills Prepared for Passive Tests.

Test No	Unit Weight (kN/m^3)	Internal Friction Angle (°)	Dilatancy Angle (°)
1	15.14	36.98	10.21
2	14.9	36.13	8.01
3	14.75	35.59	6.65
4	16.4	40.76	19.9
5	16.61	41.36	21.45
6	16.36	40.68	19.68
7	15.05	36.66	9.38
8	15.3	37.42	11.34

To obtain high density in some backfills, the backfills were compacted as shown in Figure 3.13. The test numbers prepared with compaction method are 4, 5 and 6 as illustrated in Table 7.1. The results for the calculated and measured passive lateral thrusts are shown in Table 7.2 and in Figure 7.3.

Table 7.2. The Results for the Calculated and Measured Passive Lateral Thrusts.

Test No	The Calculation Results (N)	The Measurement Results (N)	Dilatancy Angle (°)
1	2525.47	2330	10.21
2	2411.52	2080	8.01
3	2344.3	2540	6.65
4	3147.76	6390	19.9
5	3265.29	6870	21.45
6	3130.1	5820	19.68
7	2481.71	2450	9.38
8	2591.7	2730	11.34

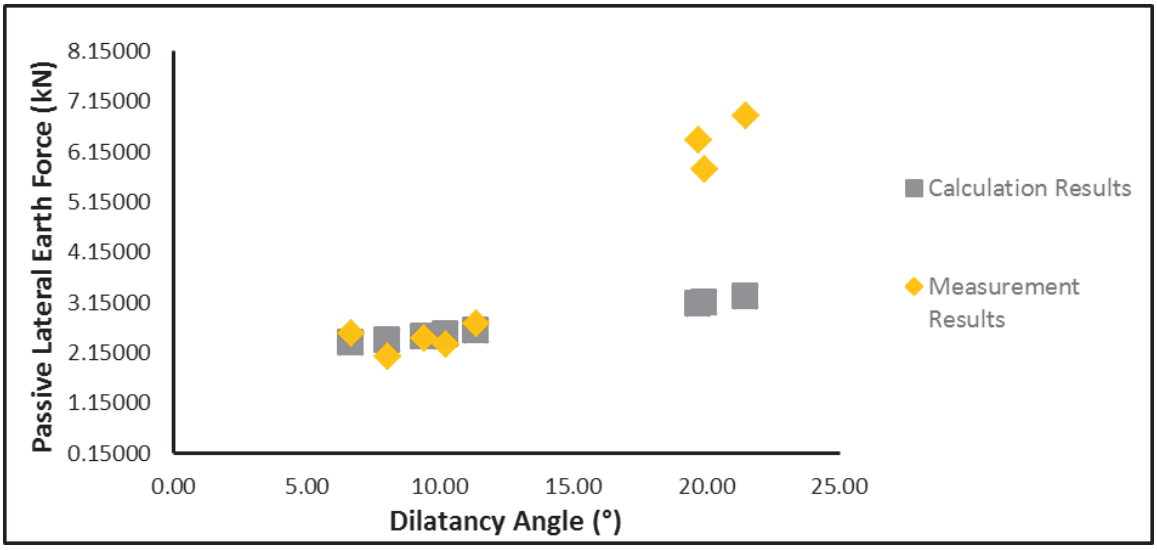


Figure 7.3. The Results for the Calculated and Measured Passive Lateral Thrusts.

As it is seen in Table 7.2 and Figure 7.3, some results are accurate while the others are not. The tests in which the results are not compatible are the tests numbered 4, 5 and 6. It means that the results for the calculated and the measured lateral thrusts are not compatible in the tests prepared with compaction. The ones for which the calculations are accurate, the backfill was prepared only by pluviation. This difference requires careful consideration.

7.6. Locked-in Stress Concept

The differences between pluviated and compacted backfills will be analyzed using a thought example. Pluviated samples' grains arrange themselves within the stack without any significant elastic deformation of grains. Therefore, each grain finds a suitable position within the soil skeleton. However, in cases where vibration plus force is applied, grains are pushed into the small void present in the underlying grain arrangements. Thus, as the individual grains are pushed between underlying grains, they deform elastically. This elastic deformation compresses the grains and the compression leads to normal forces between the grains in contact. Since grains are frictional, these additional normal forces create a frictional force that prevent individual grains from bouncing back. As a result compacted backfill becomes denser. (Figure 7.4b). The

elastic deformation of the soil particles causes an increase in lateral earth pressure coefficient at rest (K_o). This increase is shown in Figure 7.5. As it is seen in the figure, K_o values measured for compacted backfills are significantly higher. The increase lateral pressures in compacted backfills are due to the vibration and mechanical energy that resulted in elastic deformations. These elastic deformations are similar to compressed springs, thus they increase the normal stresses within the skeleton. Thus, they are referred to as locked-in stresses.

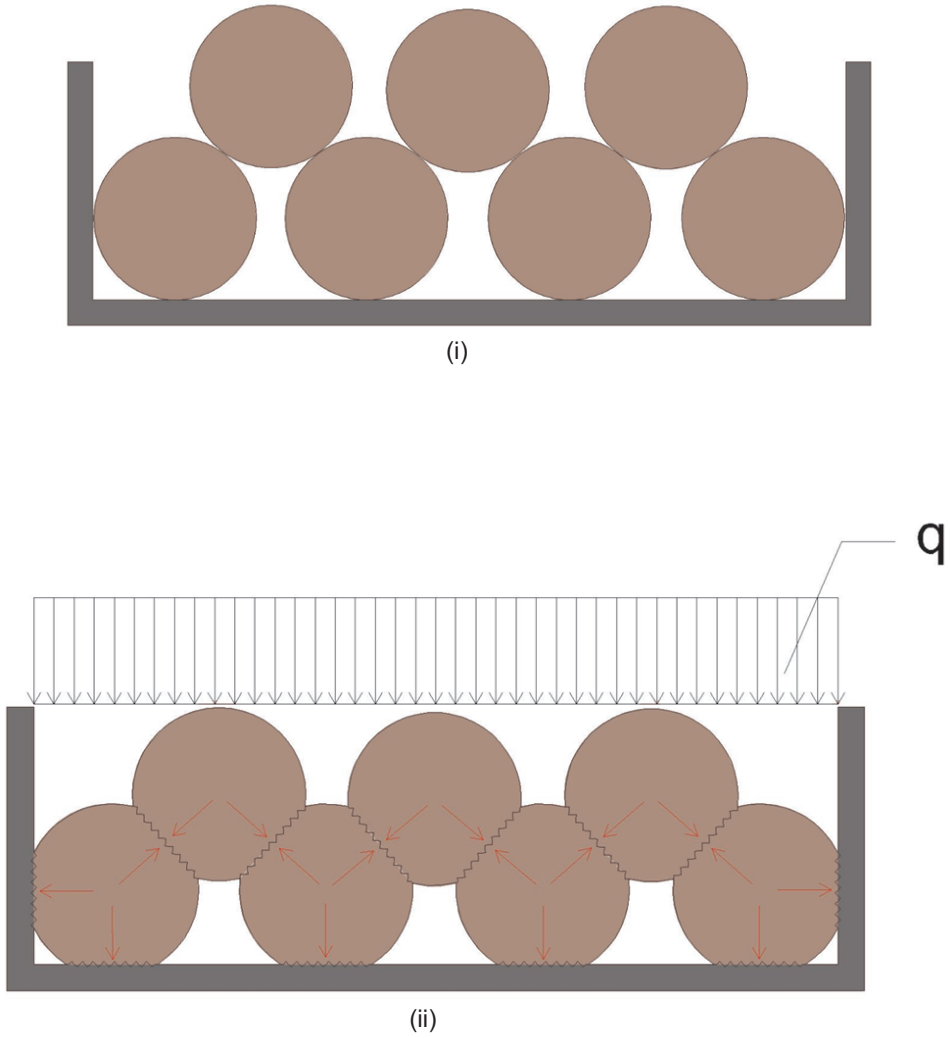


Figure 7.4. Soil Particles in a Tank (i) Before the Compaction (ii) After the Compaction.

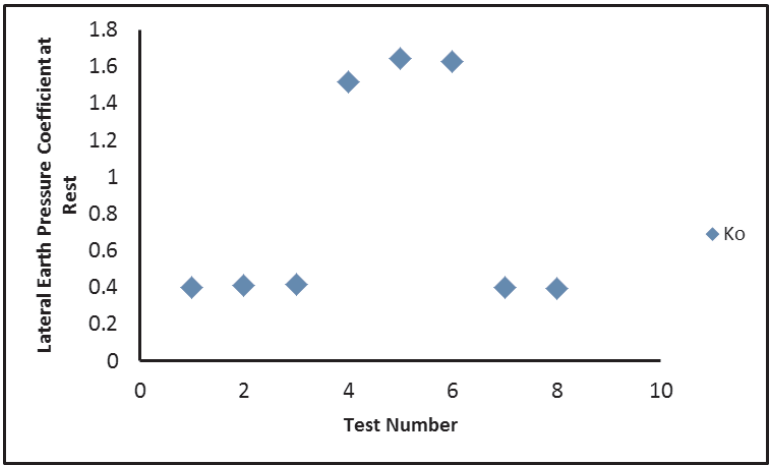


Figure 7.5. Lateral Earth Pressure Coefficient at Rest for Each Test.

Locked-in stresses increase the confining pressure of the medium. Therefore, it is no more possible to calculate confinement directly from unit weights and soil friction angles. Additionally, locked-in stresses are normal stresses acting between grains and as a result increase the strength through friction.

The magnitude of locked-in stresses should be equal to the difference of mean effective stresses at the compacted state and pluviated (normally compressed) state. Thus, locked-in stresses (1_σ) can be computed using Equation 7.6.

$$l_\sigma = ((p_i')_{comp} - (p_i')_{nc}) \tag{7.6}$$

whereis the $(p_i')_{comp}$ initial mean effective stress in compacted cohesionless soils, is the $(p_i')_{nc}$ initial mean effective stress in normally-compressed cohesionless soils.

Initial mean effective stress in compacted cohesionless soils $(p_i')_{comp}$ is calculated using Equation 7.7.

$$(p_i')_{comp} = \frac{\sigma_v' + 2 \times \sigma_h'}{3} = \frac{\sigma_v' \times (1 + 2 \times (K_o)_{comp})}{3} \tag{7.7}$$

where is the σ_v' effective vertical stress σ_h' effective horizontal stress $(K_o)_{comp}$ lateral earth pressure coefficient at rest in compacted cohesionless soils.

Effective vertical stresses σ'_v are calculated for midpoint of base of each slice because locked-in stress are determined for each slice. The effective vertical stresses at the base of n^{th} slice can be computed using Equation 7.8.

$$(\sigma'_v)_n = \gamma \times \frac{y_n + y_{n+1}}{2} \tag{7.8}$$

Overconsolidated lateral earth pressure coefficient at rest ($(K_o)_{comp}$) is specified using the data obtained the transducers mounted the wall during each test conducted on the compacted soil backfill.

Initial mean effective stress at normal consolidated state ((p'_i)) is computed using Equation 7.9.

$$(p'_i)_{oc} = \frac{\sigma'_v + 2 \times \sigma'_h}{3} = \frac{\sigma'_v \times (1 + 2 \times (K_o)_{nc})}{3} \tag{7.9}$$

where, (K_o) lateral earth pressure coefficient at rest in uncompacted cohesionless soils. This coefficient is calculated using Equation 7.10 proposed by Rankine (1857).

$$(K_o)_{nc} = 1 - \sin \phi'_p \tag{7.10}$$

After the calculation the initial mean effective stresses in compacted and uncompacted cohesionless soils, the locked-in stresses can be computed using Equation 7.6. Locked-in stresses result in higher confinement in cohesionless and frictional soils. For this reason, the influence of locked-in stresses on strength is similar to cohesion effect. Additional normal stress mobilizes friction. Thus, one has to account for an additional strength component that is equal to locked-in stress times tangent of peak friction angle. The extra strength can be added to the strength dependent on normal confinement by using Equation 7.11.

$$S_m = (S \times l_\sigma + N) \times tan\phi'_p \tag{7.11}$$

where is the S length of the base of the a slice l_σ locked-in stress at base of a slice ϕ'_p peak internal friction angle. Peak internal friction angle (ϕ'_p) is computed using Equation 2.2 proposed by Çinicioğlu and Abadkon (2014).

In the method proposed for calculation of passive lateral earth thrusts, Equation 7.4 that gives normal forces acting at bases of all the slices needs to be modified due to effect of locked-in stresses. As a result of the modification of Equation 7.4, Equation 7.12 is obtained to calculate the normal forces.

$$N = \frac{\left(\left(F_s + l_\sigma \times \tan\phi'_p \times S\right) \times \left(\sin\beta - \frac{\cos\beta \times \tan\delta \times x}{B_f}\right) + W\right)}{\left(cos\beta - tan\phi'_p \times sin\beta + \frac{\tan\delta \times x \times \left(\sin\beta + tan\phi'_p \times \cos\beta\right)}{B_f}\right)} \tag{7.12}$$

The strength that results from locked-in stresses does not have an effect on only normal forces acting at base of all the slices, but also passive lateral earth thrusts acting on the wall directly. New equation to calculate passive lateral earth thrusts that include effect of locked-in stresses is shown as Equation 7.13.

$$P \times cos\delta = \Sigma\left(N \times sin\beta\right) + \Sigma\left(S_m \times cos\beta\right) + \Sigma\left(F_S \times cos\beta\right) \tag{7.13}$$

Substituting Equation 7.11 into Equation 7.13 gives

$$\begin{aligned} P \times cos\delta = {} & \Sigma\left(N \times sin\beta\right) + \Sigma\left(\left(S \times l_\sigma \times \tan\phi'_p + N \times tan\phi'_p\right) \times cos\beta\right) \\ & + \Sigma\left(F_S \times cos\beta\right) \end{aligned} \tag{7.14}$$

By using the modified equation that includes effect of locked-in stresses, the passive lateral earth thrusts were recalculated for the compacted cohesionless backfills. The calculated and measured results in which locked-in stresses are regarded are shown in Table 7.3.

Table 7.3. The Results for the Recalculated and Measured Passive Lateral Thrusts.

Test No	The Calculation Results (N)	The Measurement Results (N)	Dilatancy Angle (°)
1	2525.47	2330	10.21
2	2411.52	2080	8.01
3	2344.3	2540	6.65
4	5200.84	6390	19.9
5	5658.01	6870	21.45
6	5368.91	5820	19.68
7	2481.71	2450	9.38
8	2591.7	2730	11.34

The calculated result-dilatancy angle and the measured result-dilatancy angle relationships are shown in Figure 7.6.

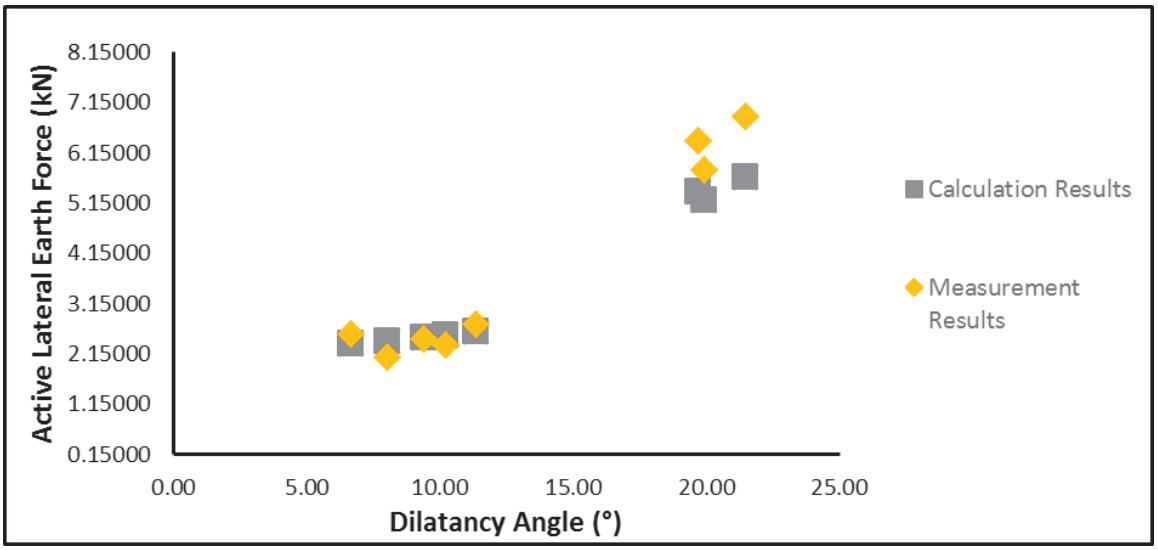


Figure 7.6. The Results for the Recalculated and Measured Passive Lateral Thrusts.

It is shown in Figure 7.6 that the calculations are very accurate.

8. DISCUSSION

8.1. Active Lateral Earth Thrusts

Both the measured active thrust values and the calculated active earth thrusts using the proposed method illustrates the influence of dilatant behavior on active forces. As expected, active lateral earth force decreases with increasing backfill dilatancy angle. The results are shown in Figure 8.1. Active forces calculated using the proposed method are compared with the results obtained through test measurements. The comparison of the calculation results and the measurement results are also given in Figure 8.1.

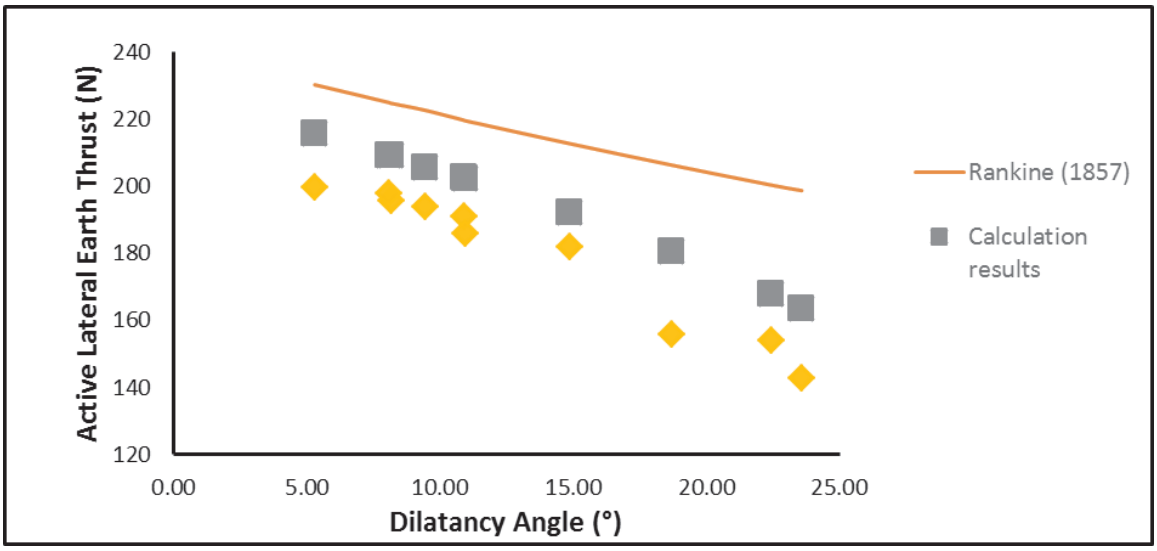


Figure 8.1. The Relationship Between Dilatancy Angle and Active Lateral Earth Thrust According to Calculation Results, Measurement Results and Rankine Theory.

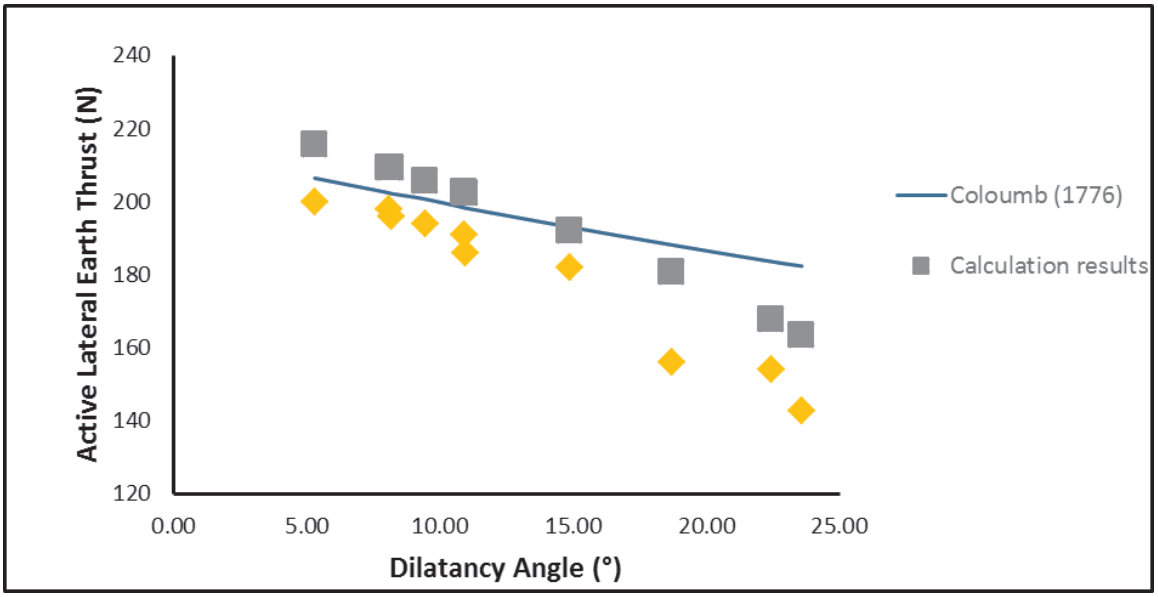


Figure 8.2. The Relationship Between Dilatancy Angle and Active Lateral Earth Thrust According to Calculation Results, Measurement Results and Coloumb Theory.

It can be seen that the calculation and measurement results are close to each other. One of the reason for the differences between them is that homogeneity of the backfill can not be controlled very precisely. Additionally, the backfill is poorly graded which complicates the measurement of test relative densities; For a poorly graded soil even the slightest mistake in the measurement of void ratios can significantly alter the calculated relative densities. Additionally, in case of 1g model tests, active pressures that act on the wall are very small. Highest measured earth pressures are on the order of 4 kPa. On the other hand, the transducers mounted on the wall have 200 kPa capacity. Thus, the cumulative influences of all these problems can affect the accuracy. However, it is observed that the results of calculation and measurement are compatible for all purposes.

The measured and calculated active thrust magnitudes are also compared with the popular earth pressure theories, namely Rankine and Coulomb methods. It is shown in Figure 8.1 and Figure 8.2, the best compatibility is between the calculation and measurement results. The results obtained from Rankine (1857) theory are bigger than the calculation and measurement results shown as in Figure 8.1. The results

obtained from Coloumb (1776) theory are about compatible with the calculation and measurement results. For all the comparisons, the components of the thrust calculations that are normal to the wall are used.

8.2. Passive Earth Thrust

Passive lateral earth thrusts acting on the wall were calculated using the method suggested for passive cases in this study. The steps are generally similar to active states. However, it is explained in Chapter 7 as that locked-in stresses must be considered in calculation of passive lateral thrusts when the backfill is compacted. When the soil is compacted, the soil particles store the work done through elastic deformations. These elastically deformed grains then act similar to compressed springs and apply normal stresses to the neighboring grains. Thus, the confining pressure within system becomes greater than the calculated confining pressure. This additional confining pressure, through the frictional behavior of intergranular contact points, increases the strength of the granular assembly with an effect similar to cohesion. This effect is more pronounced in passive problems where the wall moves towards the soil body. Thus elastically stored deformations are not reduced, they remain the same. This additional strength results in an increase in the passive thrust. Even though the increase in lateral earth pressures as a result of compaction are known, it is the first time in this study they are theoretically explained and calculated for. In this study, Equation 6.2 is proposed to numerically identify locked-in stresses that develop in the backfill. Experimental results also agree with the proposed theory and related calculation method. Locked-in stresses have significant influence on all granular materials.

Actually, locked-in stresses also develop in active cases when the backfills are prepared by compacting. However, the stresses in the backfill decrease at the moment of wall movement. Thus, an unknown proportion of the elastically stored deformations are lost. This renders them difficult to quantify. For this reason, the suggested method for the calculation of locked-in stresses could not be applied to active problems, yet. Locked-in stresses in compacted backfills at the time of active failure will be investigated in further studies.

For passive cases, the results obtained from the calculation method for the tests at different relative densities were controlled by comparing with the results of the small scale retaining wall model tests as in active states. In addition, the calculation results were compared with theories of Rankine (1857) and Coloumb (1776). As it is explained in Section 6.3, the friction forces that develop between backfills and the plexiglass surface was considered while calculating passive lateral earth thrusts according to theories of Rankine (1857) and Coloumb (1776). All the comparisons are shown in Figure 8.3 and Figure 8.4.

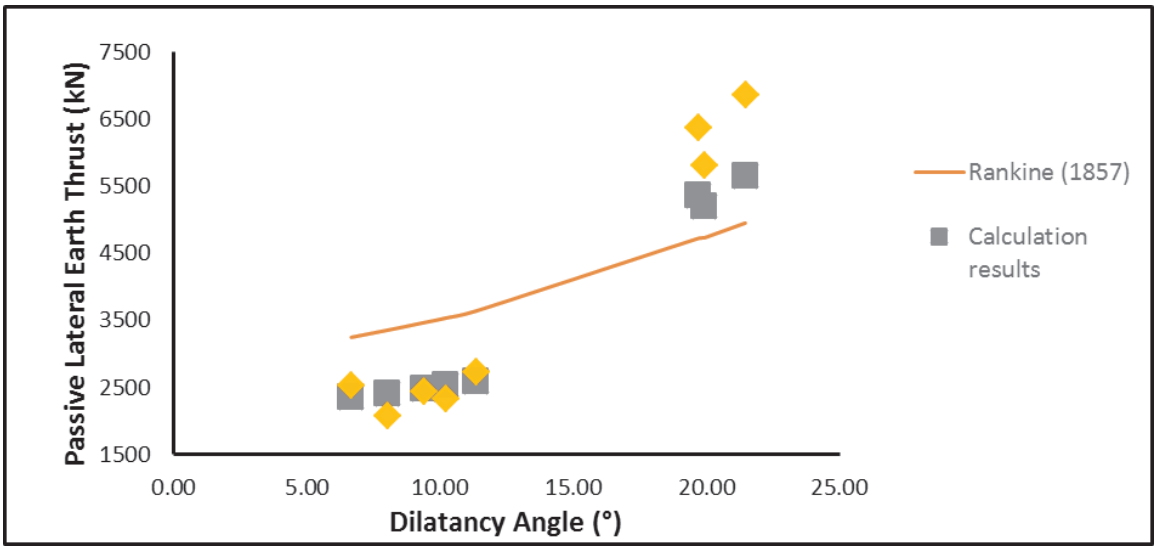


Figure 8.3. The Relationship Between Dilatancy Angle and Passive Lateral Earth Thrust According to Calculation Results, Measurement Results and Rankine Theory.

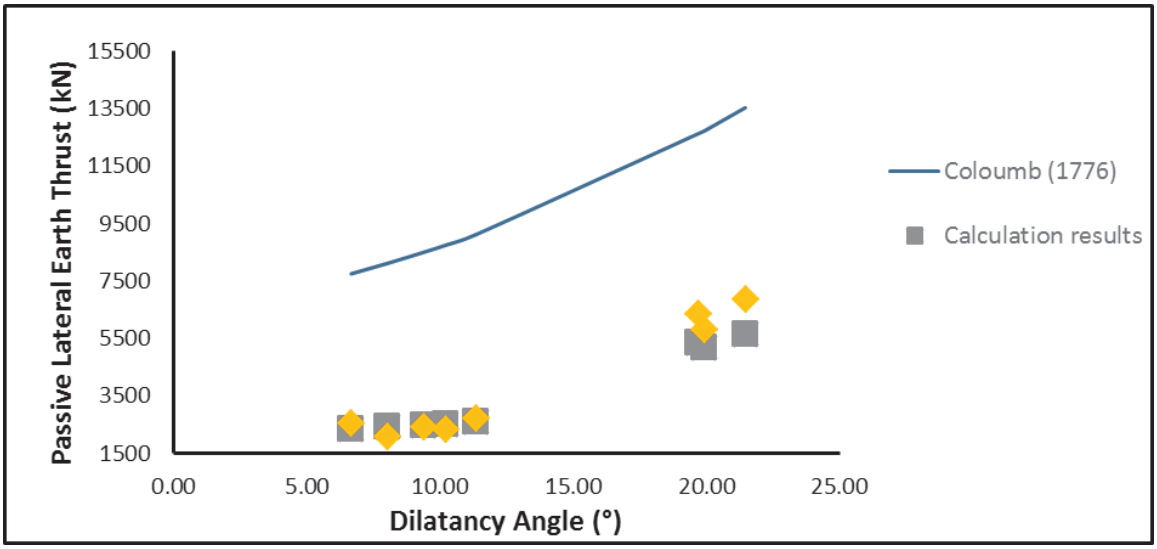


Figure 8.4. The Relationship Between Dilatancy Angle and Passive Lateral Earth Thrust According to Calculation Results, Measurement Results and Coloumb Theory.

As a result of all the comparisons, it can be said that there is a compatibility between the calculated and measurement results as shown in Figure 8.3 and Figure 8.4. The results for passive lateral earth thrusts calculated using Coloumb (1776) theory are so greater than the calculated and measured results as shown in Figure 8.4. The relationship between the Rankine (1857) results and, the results of calculation and measurement can be separated in two groups: for uncompacted and compacted soils. In uncompacted soils, the calculated and measured results are smaller than the results obtained from Rankine (1857) theory. However, the results of calculation and measurement are greater than the Rankine (1857) theory results. The result for this difference is locked in stress concept. The method of Rankine (1857) theory does not include the effect of locked in stresses.

9. CONCLUSIONS

This study attempts to quantify the influence of dilatancy angle on ultimate lateral earth pressures. For this purpose, a new method that considers the influence of dilatancy angle on the failure planes was incorporated into the conventional slice methods. Resulting equations were used to compute ultimate earth thrusts. Model tests were conducted to test the accuracy of the proposed method. Computed and measured values show good agreement. Moreover, it has been shown that the proposed method is more accurate than conventionally used methods of calculation.

Additionally, a new concept regarding the behavior of granular assemblies is proposed referred to as locked-in stresses. Within this thesis, locked-in stresses were quantitatively identified at the first time. This quantitative identification enables correct calculation of passive lateral earth thrusts for especially compacted soils.

REFERENCES

Altunbaş, A., 2014, "Influence of Dilatancy on Slip Planes and on Localization of Strains", Ph.D. Thesis, Bogaziçi University.

American Society for Testing and Materials, 2006, "Standard Test Methods for Minimum Index Density and Unit Weight of Soils and Calculation of Relative Density", *ASTM Standards: D4254*.

Atkinson, J.H., 1981, *Foundation and Slopes: An Introduction to Applications of Critical State Soil Mechanics*, John Wiley and Sons, Inc., NY, USA.

Bardet, J.P., 1997, *Experimental Soil Mechanics*, Prentice Hall, NJ, USA.

Bishop, A.W., 1955, "The use of the Slip Circle in the Stability Analysis of Slopes", *Geotechnique*, Vol. 5, pp. 7-17.

Bolton, M.D., 1986, "The Strength and Dilatancy of Sands", *Geotechnique*, Vol. 36, No. 1, pp. 65-78.

Chen, Z., S. Li, 1998, "Evaluation of Active Earth Pressure by the Generalized Method of Slices", *Canadian Geotechnical Journal*, Vol. 35, pp. 591-599.

Çinicioğlu, O., A. Abadkon, A. Altunbaş, and M. Abzal, 2013, "Variation of Friction Angle and Dilatancy for Anisotropic Coheisonless Soils", *Paris: Proceedings, 18th International Conference on Soil Mechanics and Geotechnical Engineering.*

Çinicioğlu, O., A. Abadkon, 2014, "Dilatancy and Friction Angles Based on in Situ Soil Conditions", *Journal of Geotechnical and Geoenvironmental Enginnering*, 10.1061/(American Society of Civil Engineering)GT.1943-5606.0001272 , 06014019.

Coulomb, C.A., 1776, "Essai Sur Une Application Des Regles de Maximis et Minimis'a Quelques Probl'emes de Statique", *Relatifs'a l'Architecture*, Memoires de

l'Academie Royale Pres Divers Savants, Vol. 3, pp. 343-382.

Fan, K. 1983, "Evaluation of the Interslice Side Forces for Lateral Earth Force and Slope Stability Problems", M.Sc. Thesis, University of Saskatchewan.

Fellenius, W., 1936, "Calculation of the stability of earth dams", *Proceedings of the Second Congress on Large Dams*, Vol. 4, pp. 445-463.

Fredlund, D.G., J. Krahn, and D.E. Pufahl, 1981, "The Relationship Between Limit Equilibrium Slope Stability Methods", *In Proceedings of the International Conference on Soil Mechanics and Foundation Engineering*, Stockholm, Sweden, Vol. 3, pp. 409-416.

Goel, S., N.R. Patra, 2008, "Effect of Arching on Active Earth Pressure for Rigid Retaining Walls Considering Translation Mode", *International Journal of Geomechanics*, American Society of Civil Engineering, Vol. 8, No. 2, pp. 123-133.

Handy, R.L., 1985, "The arch in soil arching", *Journal of Geotechnical Engineering*, American Society of Civil Engineering, Vol. 111, No. 3, pp. 302-318.

Hanna, A., I. Al-Khoury, 2005, "Passive Earth Pressure of Overconsolidated Cohesionless Backfill", *Journal of Geotechnical and Geoenvironmental Engineering*, American Society of Civil Engineering, Vol. 131, No. 8, pp. 978-986.

Jackson, P., 2010, "An experimental Study on Geosynthetic Reinforced Soil Walls Under Seismic Loading", University of Canterbury, Christchurch, NZ.

Janssen, H.A., 1895, "Versuche Über Getreidedruck in Silozellen", Zeitschr Vereines Deutscher Ingenieure, Vol. 39, No. 35, pp. 1045-1049.

Janbu. N., L. Bjerrum, and B. Kjaernsli, 1956, "Stabilitetsberegning for Fyllinger Skjaeringer Og Naturlige Skraninger", *Norwegian Geotechnical Publication*, No. 16, Oslo, Norway.

Janbu, N., 1957, "Earth Pressure and Bearing Capacity Calculations by Generalized Procedure of Slices", *Proceedings, 4th Int. Conf. on Soil Mechanics and Foundations Engineering, London*, No. 2, pp. 207-212.

Morgenstern, N. R., and V.E. Price, 1965, "The Analysis of the Stability of General Slip Surfaces", *Géotechnique*, Vol. 15, No. 1, pp. 79-93.

Niedostatkiewicz, M., D. Les'niewska, and J. Tejchman, 2011, "Experimental Analysis of Shear Zone Patterns in Sand During Earth Pressure Problems Using Particle Image Velocimetry", *Strain*, Vol. 47, pp. 218-231.

Paik, K.H., and R. Salgado, 2003, "Estimation of Active Earth Pressure Against Rigid Retaining Walls Considering Arching Effects", *Geotechnique*, Vol. 53, No. 7, pp. 643-53.

Rahardjo, H., 1982, "Lateral Earth Force Calculations using Limit Equilibrium", M.Sc. Thesis, University of Saskatchewan.

Rahardjo, H., and D.G. Fredlund, 1984, "General Limit Equilibrium Method for Lateral Earth Force", *Canadian Geotechnical Journal*, Vol. 21, pp. 166-175.

Rankine, W.M.J., 1857, "On Stability on Loose Earth", *Philisophic Transactions of Royal Society*, London, Vol.1, pp. 9-27.

Spencer, E., 1967, "A Method of Analysis of the Stability of Embankments Assuming Parallel Inter-Slice Forces", *Geotechnique*, Vol. 17, pp. ll-26.

Spangler, M.G., and R.L. Handy, 1984, *Soil Engineering*, Harper and Row, New York.

Terzaghi, K., 1936, "A Fundamental Fallacy in Earth Pressure Computations", *Journal of the Boston Society of Civil Engineers*, Vol. 23, No. 2, pp. 71-88.

Terzaghi, K., and R.B. Peck, 1967, *Soil Mechanics in Engineering Practice, 2nd Ed.*, Wiley, New York.

Shields, D.H., and Z.A. Tolunay, 1972, "Passive Pressure Coefficients for Sand", *Canadian Geotechnical Journal*, Vol. 9, pp. 501-503.

Shields, D.H., and Z.A. Tolunay, 1973, "Passive Pressure Coefficients by Method of Slices", *Journal of the Soil Mechanics and Foundations Division*, American Society of Civil Engineering, Vol. 99, No. 12, pp. 1043-1053.

Vaid, Y.P., and S. Sasitharan, 1992, "The Strength and Dilatancy of Sand", *Canadian Geotechnical Journal*, Vol. 29, pp. 522-526.

White, D.J., W.A. Take, and M.D. Bolton, 2003, "Soil Deformation Measurements Using Particle Image Velocimetry PIV and Photogrammetry", *Geotechnique*, Vol. 53, pp. 619-631.